Free boundary problem for cell protrusion formations: theoretical and numerical aspects

Olivier Gallinato, Masahito Ohta, Clair Poignard, Takashi Suzuki

Free boundary problem for cell protrusion formations: theoretical and numerical aspects

Olivier Gallinato, Masahito Ohta, Clair Poignard, Takashi Suzuki

RESEARCH REPORT
N° 8810
November 2015
Project-Team MONC

ISSN 0249-6399 ISRN INRIA/RR--8810--FR+ENG

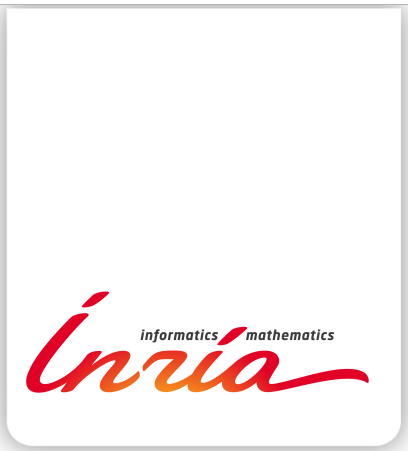

Free boundary problem for cell protrusion formations: theoretical and numerical aspects

Olivier Gallinato*, Masahito Ohta†, Clair Poignard*, Takashi Suzuki‡

Project-Team MONC

Research Report n° 8810 — November 2015 — 36 pages

Abstract: In this paper, we derive a free boundary problem for cell protrusion formation in which the cell membrane is precisely described thanks to a level-set function, whose motion is due to specific signalling pathways. The model consists in Laplace equation with Dirichlet condition inside the cell coupled to Laplace equation with Neumann condition in the outer domain. The motion of the interface is due the gradient of the inner quantity. We prove the well-posedness of our free boundary problem under a sign condition on the datum similarly to the Taylor criterion in water waves. We also propose an accurate numerical scheme to solve the problem and we exhibit the main biological features that can be accounted for by the model. Even though simplistic from the modeling point of view, we claim that this paper provides the theoretical and numerical grounds for single cell migration modeling. In particular, specific chemical reactions that occured at the cell membrane could be precisely described in forthcoming works.

Key-words: Mathematical Biology, Cell Protrusion Formation, Free boundary problem, Finite differences on Cartesian grids
65M06, 65M12, 92C37

Corresponding author: Clair.Poignard@inria.fr

* Team MONC, INRIA Bordeaux-Sud-Ouest, Institut de Mathématiques de Bordeaux, CNRS UMR 5251 & Université de Bordeaux, 351 cours de la Libération, 33405 Talence Cedex, France.
† Department of Mathematics, Tokyo University of Science, Tokyo, Japan.
‡ Division of Mathematical Science, Osaka University, Osaka, Japan.

RESEARCH CENTRE
BORDEAUX – SUD-OUEST

200 avenue de la Vieille Tour
33405 Talence Cedex

Problème à frontière libre pour la formation de protrusions à l'échelle de la cellule: Aspects théoriques et numériques

Résumé : Nous présentons un modèle à frontière libre pour modéliser la formation de protrusions à l'échelle de la cellule. La membrane cellulaire est décrite à l'aide d'une fonction level-set dont le mouvement est dû au gradient d'un signal chimique. Le modèle consiste en un couplage entre une équation de Laplace avec condition de Dirichlet dont la donnée est la trace sur l'interface de la solution d'un problème de Laplace avec condition de Neumann dans le domaine extérieur. La vitesse de la frontière libre est proportionnelle au gradient du signal intérieur à la cellule ce qui génère *a priori* une perte de régularité. Nous prouvons le caractère bien posé de ce modèle sous une condition de signe similaire au critère de Taylor pour les "water waves" et nous présentons une méthode aux différences finies pour résoudre précisément le problème à frontière libre. Bien que simple, notre modélisation présente les bases d'une modélisation fine des formations de protrusion à l'échelle de la cellule.

Mots-clés : Mathématiques pour la biologie, Formation de Protrusion, Problème à frontière libre, Différences finies
65M06, 65M12, 92C37

Contents

1 Introduction

Invadopodia and *pseudopodial protrusions* are elongated shapes, which are formed during cell invasion and mesenchymal migration. These phenomena are the crucial points in the metastasic process, which is the major cause of death from cancer. Even though these phenomena are different from the biological point of view, both involve specific signaling pathways occuring on the cell membrane. The aim of this paper is to present a simple free boundary model, which can be seen as the main basis to model such phenomena at the cell scale. The main novelty lies in the fact that the cell membrane is precisely accounted for as a free boundary, whose motion is driven by the gradient of a chemical signal. In this paper, we study theoretically and numerically the *core* model of protrusion formation at the cell scale. Note that our model is somehow related to Stefan-type models: in Appendix A we show how well-posedness of the quasistatic 2–phase Stefan model can be tackled thanks to our approach.

1.1 Motivations

Early-stage carcinoma are mostly confined to epithelium, which is separated from the underlying tissue by a basement membrane composed of dense fibers of extracellular matrix. In order to

cross this tight barrier, metastatic cells use a complex internal machinery, named *invadopodia*, which lies on the actin polymerization and that leads to the formation of proteolytic, protrusive and very localized subcellular structures. Saitou *et al.* derive a model at the cell level for the formation and the maturation of invadopodia [18]. They describe the distribution of specific enzymes, called Matrix Metalloproteinases (MMPs), which degrade the extracellular matrix, creating then ligands. These ligands, when bound to the membrane receptors, generate a signal which polymerizes the actin, leading to the formation of the *invadopodium*. Figure 1 provides an

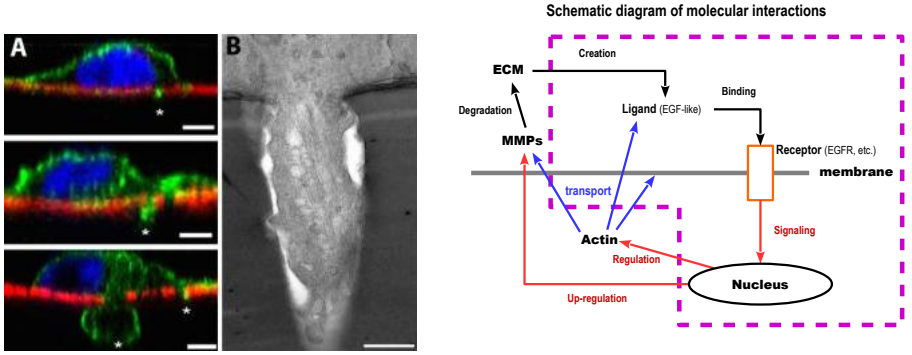

(a) Experiment showing the formation of an invadopodium [19].

(b) Molecular interactions involved in the invadopodia model of Saitou *et al.* The dashed line shows the processes we focus on in this article.

Figure 1: Invadopodia.

experimental visualization of invadopodia and the schematic diagram of the involved chemical reactions, as explained by Saitou *et al.* [18].

Once the basement membrane has been crossed, cells adopt a migratory behavior to progress in the conjonctive tissue by projecting wider elongated protrusions. Cells that migrate on a 2D extracellular matrix form flat and plated structures called *lamellipodia*, at the leading edge, whereas they show various shapes in 3D migration, in particular cylindrical pseudopodia (see [4] for a biological review of migration process, and Figure 2). These structures result also from

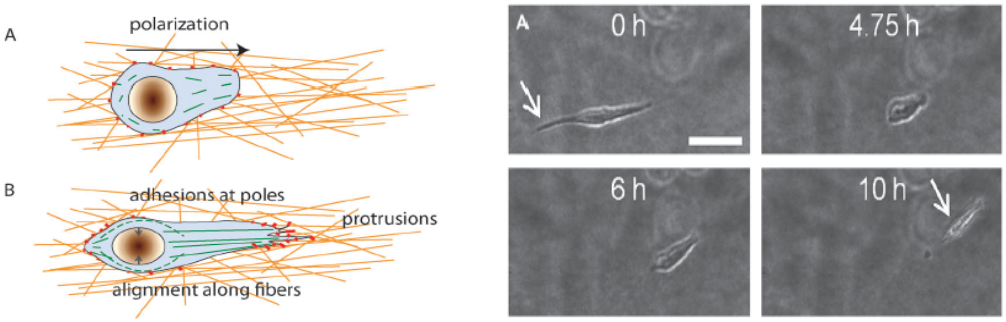

Figure 2: Extended pseudopodial protrusion in 3D extracellular matrix, taken from [16].

both actin polymerization and cytoskeleton reorganization, as for invadopodia, but they grow as a response to a weak external gradient of chemoattractants, which are released by neighboring blood vessels. Mesenchymal protrusions are wide directional migration structures, at the cell

scale, while invadopodia are local subcellular structures that are needed to perforate and pass through collagen walls.

As far as we know, most of the current models for such phenomena do not discriminate between the interior and the exterior of the cell. More precisely, in cell migration models – see for instance [10] – the cell membrane is implicitly determined by the actin concentration, which satisfies a reaction–diffusion equation. The main drawbacks of these approaches lie in the fact that specific membrane receptors and ion channels such as Na^+/H^+ exchangers or sodium channels that might be crucial in cell migration – see Stock and Schwab [21] and Yang *et al.* [22] – cannot be considered. Moreover, in the numerical simulations, the cell shape, and thus the resulting protrusion, depends arbitrarily on the threshold of detection of the actin. Since the main mechanisms involved in protrusion formation are tightly linked to the cell membrane, the present paper aims at providing the grounds for a cell modeling that describes precisely the membrane motion. It is worth noting that our goal is to provide the theoretical and numerical bases of the modeling, and therefore we only deal with a *core* model, which takes the membrane into account, and which will be enriched by more biological features in following research.

More precisely, we derive a free boundary problem in which the cell membrane is given by the zero of a level set function, whose motion is due to specific signalling pathways. This makes it possible to account precisely for protusion formation. More precisely, the motion of the level set is driven by the gradient of a chemical signal produced by (and inside) the cell as a response to the detection on the cell membrane of extracellular ligands (for invadopodia) or chemoattractants (for pseudopodial structures). In the case of invadopodia, MMP enzymes are embedded in the cell membrane and degrade the extracellular matrix by contact, creating a ligand flux, while for pseudopodia, the source of chemoattractant diffuses far from the cell membrane. For the sake of simplicity, and since we are mainly concerned in the membrane description, we do not consider the production of MMPs: we assume that the ligand is created by a local concentration of MMP, which is a given Gaussian function on the interface. In the case of pseudopodial structures, chemoattractants are diffusing from a neighboring blood vessel and create an external gradient that leads to the cell polarization: proteins that are involved in actin polymerization are advected towards the leading edge of the cell. Thus, pseudopodium-like protrusion modeling needs to take the protein localization into account. As for MMPs, our model is simplified by considering a given function for the protein localization. Introducing this function and modifying the data, pseudopodia model will be similar to invadopodia model. In each biological situation, more realistic complexification of the model will be addressed in forthcoming works, without changing the main structure of the model.

1.2 Simple model for protrusion formation and main results

Our model describes the protrusion formation process. It is schematized by the scheme of Figure 3: for a given distribution of MMP enzymes, a flux of ligands $c^\star$ resulting from the matrix degradation is generated on the boundary of the membrane. These ligands diffuse in the extracellular medium and, when bound to the cell membrane, generate a signal σ, which diffuses inside the cell. The membrane motion is then driven by the velocity, which is given by the gradient of the signal. More precise models, that involve the production of MMP enzymes and other complex biological phenomena such as precise actin polymerization, as modeled by Mogilner [13] for instance, are not addressed in this paper. The new insight of the modeling lies in the description of the cell membrane as a free-boundary, which is driven by the gradient of a specific chemical signal: the membrane location is an unknown of the PDE systems, and does not result *a posteriori* from the actin concentration.

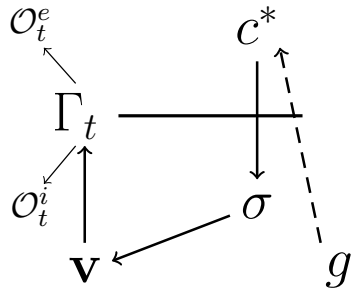

Figure 3: Schematic diagram of the molecular interactions involved in our model

1.2.1 Mathematical statement of the model

Let Ω be a bounded domain of $\mathbb{R}^2$, with smooth boundary $\partial\Omega$. Denote by Γ_0 the initial location of the cell membrane parameterized by ζ_0, which is assumed to be smooth enough. Let g be a given function, smooth enough, defined in $\mathbb{R}^+ \times \Omega$, which corresponds to the concentration of MMPs. The location of cell membrane Γ_t is supposed to be parameterized by the counter-clockwisely oriented vector-field ζ and we define respectively by $\mathcal{O}_t^i$ and $\mathcal{O}_t^e$ the cell cytoplasm and the extracellular domain, see Figure 4.

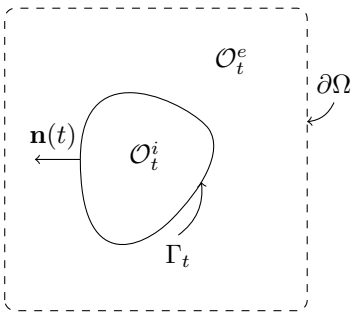

Figure 4: Geometry of the problem. The cell $\mathcal{O}_t^i$ is imbedded in the bath $\mathcal{O}_t^e$. The whole domain Ω does not depend on the time variable. It is defined by $\Omega = \mathcal{O}_t^e \cup \overline{\mathcal{O}_t^i}$.

The PDE system satisfied by ζ, $c^\star$, and σ reads

$$\zeta|_{t=0} = \zeta_0, \quad \text{and} \quad \partial_t \zeta = \nabla\sigma(\zeta(t,\theta)), \quad \forall t > 0, \ \ \forall \theta \in \mathbb{R}/2\pi\mathbb{Z}, \tag{1a}$$

where $\forall t \geq 0$, one has

$$\Delta c^\star = 0, \quad x \in \mathcal{O}_t^e, \tag{1b}$$
$$c^\star|_{\partial\Omega} = 0, \quad -\partial_{\mathbf{n}} c^\star|_{\Gamma_t} = g|_{\Gamma_t}, \tag{1c}$$
$$\Delta\sigma = 0, \quad t \in [0,T], \ \ x \in \mathcal{O}_t^i, \tag{1d}$$
$$\sigma|_{\Gamma_t} = c^\star|_{\Gamma_t}. \tag{1e}$$

Here above $\mathcal{O}_t^i$ denotes the domain enclosed by $\zeta(t,\cdot)$, and we define $\mathcal{O}_t^e = \Omega \setminus \overline{\mathcal{O}_t^i}$.

Remark 1 (Eulerian formulation)**.** *Another interesting way to formulate equation* (1a)*, especially for numerical purposes, is to use the Eulerian framework:* Γ_t *is then described as the zeros*

of a level set function $\psi(t,\cdot)$ defined in Ω, and whose transport is given by

$$(\partial_t + \nabla\sigma\cdot\nabla)\psi = 0 \quad t\in[0,T],\ \ x\in\mathcal{O}_t^i, \tag{2}$$

and then the inner and outer domains are simply given as

$$\begin{aligned}\mathcal{O}_t^i &= \{x\in\Omega : \psi(t,x) > 0\},\\ \mathcal{O}_t^e &= \{x\in\Omega : \psi(t,x) < 0\},\\ \Gamma_t &= \{x\in\Omega : \psi(t,x) = 0\}, \qquad \mathbf{n} = -\frac{\nabla\psi}{|\nabla\psi|}.\end{aligned}$$

Such Eulerian formulation makes it possible to use in a simple way Finite Difference schemes on Cartesian grids. The numerical methods used in our simulations as well as the results are precisely described in Section 3.

Remark 2. *Model* (1) *holds for invadopodia formation, since the MMPs generate an outer flux of ligands. For pseudopodia formation, the chemoattractant diffuses far from the membrane, and the proteins that amplify the signal are localized at the front of the cell, through a complex chemical process described by Ridley et al. in [17]. Therefore, the boundary conditions* (1c) *and the advection equation* (1a) *should be replaced respectively by*

$$c^\star|_{\partial\Omega} = g, \quad \partial_{\mathbf{n}} c^\star|_{\Gamma_t} = 0, \tag{3a}$$

$$\partial_t\zeta = \kappa\,\nabla\sigma(\zeta(t,\theta)) \quad t\in[0,T], \tag{3b}$$

where g denotes now the source of chemoattractant in the extracellular domain, and κ is a smooth positive function, which localizes the cytoplasmic proteins that amplify the signal inside the cell. These modifications in the model given by (3) *will be included in pseudopodia simulations, but they do not change the well-posedness result.*

1.2.2 Well-posedness under specific sign condition

From the theoretical point of view, we first state that our free boundary problem is well-posed under a specific sign condition on the data.

Theorem 3 (Well-posedness of the problem)**.** *Let Ω be a smooth domain of $\mathbb{R}^2$ which strictly contains the unit disk, and denote by Γ_0 the initial location of the membrane, given as a perturbation of the unit circle : $\Gamma_0 = \{e^{i\theta} + \xi_0(\theta),\ \theta\in\mathbb{T}\}$.*

Let $s\geq 3$, and let $g\in W^{1,\infty}(\mathbb{R}^+; H^{s+1/2}(\Omega))$ such that for a given $\alpha > 0$,

$$g(t,x)\geq\alpha > 0. \tag{4}$$

There exist $M > 0$ and $T > 0$ small enough such that if

$$\|\xi_0\|_{H^s(\mathbb{T})}\leq M,$$

then, there exists a unique solution $(\zeta, c^\star, \sigma)$ on $(0,T)$ to problem (1) *such that*

$$\zeta\in L^\infty(0,T;H^s(\mathbb{T}))\cap L^2(0,T;H^{s+1}(\mathbb{T})),$$

and for almost any $t\in(0,T)$,

$$c^\star\in H^{s+1/2}(\mathcal{O}_t^e)\,, \qquad \sigma\in H^{s+1/2}(\mathcal{O}_t^i).$$

Remark 4 (On the assumption of small data and the bidimensional framework)**.** *We provide the proof in a bidimensional framework and using the tools of Nalimov, Yosihara, and Iguchi [14, 23, 6]. We are confident that the result holds in 3D thanks to more complex tools, but this is not the aim of the paper, which mainly deals with modeling. In addition, according to the papers of Lannes et al., the smallness assumption on the H^s norm of the datum g seems technical. However we prefer to present this point of view to provide the heuristics of the quasilinearization. It is also worth noting that the approach we choose in this paper is valid only for the bidimensional case in which complex analysis provides a nice tool to define the integral operators. The extension of Theorem 3, without smallness assumption in the 3D, using the advanced and technical tools developed by Lannes will be investigated in forthcoming works.*

1.2.3 Numerical simulations illustrating biological phenomena

Let present here the main phenomena that can be accounted for by the model.
A plot of an invadopodium simulation is provided in Figure 5. An accumulation of ligands (dark grey) can be observed around the membrane area where MMP enzymes are concentrated (Fig. 5(a)). Consequently, the signal accumulates in the adjacent cytoplasmic area (Fig. 5(b)), and leads to the actin polymerization and thus invadopodium growth. Obviously, the simplified

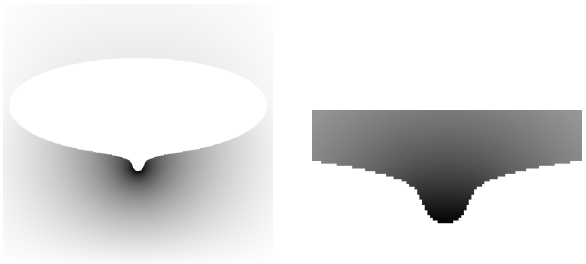

(a) Ligand diffusion.

(b) Focus on the invadopodium.

Figure 5: Invadopodia simulation.

model gives simplified results, particularly as regards the protrusion shape. For example, as the diffusion of the signal generates a smooth velocity, the membrane is rounded at the root of the invadopodium, unlike what is observed in biological experiments (Figure 1). Figure 6 shows a simulation of a pseudopodial projection, at the leading edge of the cell, in response to a chemotactic signal which is diffused from the right boundary of the domain. Both simulations

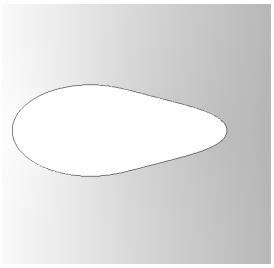

Figure 6: Simulation of a pseudopodial projection.

give an idea of the various changes in morphology of metastatic cancer cell during the invasion

and migration. Finally, note that both processes can be concomittents (*filipodes* at the front of the pseudopodial protrusion) and that critical processes involved in migration (binding to collagen fibers at the front of the pseudopodial protrusion, myosin-dependent retraction of the cell rear) are not considered in this study.

1.3 Outline of the paper

The main difficulties from both theoretical and numerical point of view lies in the fact that the velocity of the cell membrane is driven by the gradient of the signal σ, which leads to an *a priori* loss of regularity (and thus a loss of numerical accuracy). The aim of this paper is to provide the tools to tackle such difficulties.

We first present in Section 2 the main arguments that lead to well-posedness in 2D. They are based on the same arguments as Yosihara's and Iguchi's approaches [6, 23], taking advantage of the bidimensional configuration. Thanks to the Lagrangian formulation and the use of complex analysis tools we provide the Dirichlet-to-Neumann operators in both inner and outer domains that make it possible to rewrite equivalently the free boundary problem on the torus $\mathbb{R}/2\pi\mathbb{Z}$ as provided in Lemma 11. We then perform a quasilinearization of this equivalent problem in Subsection 2.1, which leads to the well-posedness result under a sign condition of the datum g. The sign condition under which holds the well-posedness is similar to the Taylor criterion in water waves [9, 23, 6] under which Taylor instabilities occurs. We conclude by presenting the numerical methods we use to compute our model in Section 3. We illustrate numerically that instabilities appear if the positivity of g is not satisfied and we show numerically the protrusions formation. In Appendix A we show how the well-posedness of the quasistatic 2–phase Stefan model can be tackled thanks to our approach.

2 Mathematical analysis

In order to prove the well-posedness of Problem (1), we use the same strategy as developed by Yosihara and Iguchi in [23, 6]. More precisely, using the Lagrangian form of Problem (1), we prove the well-posedness for small data around the unit circle, meaning that the free boundary $\gamma(t)$ for $t \in [0,T]$ is in a neighborhood of the unit circle Γ_0:

$$\gamma_0 = \{\zeta_0(\theta) := e^{i\theta}, \quad \theta \in [0, 2\pi]\}.$$

Let parameterize Γ_t by ζ as

$$\Gamma_t = \{\zeta(t,\theta) := \zeta_0(\theta) + \xi(t,\theta), \quad \theta \in [0,2\pi]\}\,. \tag{5}$$

The outward normal $\mathbf{n}$ to Γ is given by

$$\mathbf{n} = \frac{1}{|\partial_\theta \zeta|}\partial_\theta \zeta^\perp, \quad \text{with} \quad \partial_\theta \zeta^\perp = \begin{pmatrix} \partial_\theta \zeta_2 \\ -\partial_\theta \zeta_1 \end{pmatrix} = \partial_\theta \zeta_0^\perp + \partial_\theta \xi^\perp.$$

For the sake of simplicity, we suppose that the outer boundary $\partial\Omega$ of Ω is the circle of radius $R_0 > 1$. As shown in [6], the following proof can be extended to other smooth geometries but this complexifies the calculations.

We introduce the following useful notations:

Notation 5. *We generically denote by L^2 and H^s, for $s \geq 0$, the Lebesgue space $L^2(\mathbb{T})$ and the Sobolev space $H^s(\mathbb{T})$, respectively.*

- *For any $f \in L^2(\mathbb{T})$, we denote by $\hat{f}_k$ its k^{th}-Fourier coefficient defined by*

$$\hat{f}_k = \frac{1}{2\pi}\int_0^{2\pi} f(\theta)e^{-ik\theta}d\theta.$$

- *H^s is then defined by*

$$H^s = \left\{ f \in L^2(\mathbb{T}), \quad \sum_{k\in\mathbb{Z}}(1+|k|^2)^s|\hat{f}_k|^2 < +\infty \right\}$$

- *We denote by $\mathcal{P}_0$ the projection on the constants:*

$$\mathcal{P}_0 f := \frac{1}{2\pi}\int_0^{2\pi} f(\varphi)\,d\varphi = \hat{f}_0, \quad \forall f \in L^2.$$

- *The Hilbert transform $\mathcal{H}$ is the zeroth order operator defined as*

$$\mathcal{H}f := \sum_{k\in\mathbb{Z}}(-i\,\mathrm{sgn}\,(k))\hat{f}_k e^{ik\theta}, \quad \forall f \in L^2.$$

- *For $\lambda > 0$, we denote by $R_0^{-\lambda|D|}$ the smoothing operator*

$$R_0^{-\lambda|D|} f := \sum_{k\in\mathbb{Z}} R_0^{-\lambda|k|}\hat{f}_k e^{ik\theta}.$$

We remind the definition of the functional spaces $L_0(r,s\,;\tau)$ introduced by Yosihara (Definition 4.21 at page 70 of [23]):

Definition 6 (The spaces $L_0(r,s\,;\tau)$ of Yosihara [23])**.** *Let $s > 0$ and $(r,\tau) \in [0,s]^2$.*

We say that an operator $\mathcal{B}(\xi)$ depending on $\xi := (\xi_n)_{n=1,\cdot,4} \in (H^s)^4$ belongs to $L_0(r,s\,;\tau)$ if there exist $C_s > 0$ and $C_\tau > 0$ such that the following two estimates hold

$$\|\mathcal{B}(\xi)f\|_s \leq C_s\|\xi\|_s\|f\|_r, \quad \forall f \in H^r,\, \forall \xi \in (H^s)^4 \,s.t.\, \|\xi\|_s \leq C_s,\, \|\xi\|_\tau \leq C_\tau, \tag{6a}$$

and for any $(\xi^0,\xi^1) \in (H^s)^4 \times (H^s)^4$ such that $\|\xi^j\|_\tau \leq C_\tau$, and $\|\xi^j\|_s \leq C_s$, for $j = 0,1$:

$$\|\mathcal{B}(\xi^0)f - \mathcal{B}(\xi^1)f\|_s \leq C_s\|\xi^0 - \xi^1\|_s\|f\|_r, \quad \forall f \in H^r. \tag{6b}$$

The following lemma links the tangent and the normal components of the gradients of c and σ, solutions at any time of the time-independent elliptic problems (1b)–(1c) and (1d)–(1e) respectively. Therefore we fix the variable t and omit it in the notations.

Lemma 7 (Linking the normal component of the gradient to the tangent component)**.** *Let $s \geq 3$. Let ζ be defined by (5), with ξ smooth enough. Let $c^\star$ and σ be the solutions to (1b)–(1c) and (1d)–(1e) respectively.*

There exist two 0^{th}-order operators $\mathcal{L}_\mathrm{i}$ and $\mathcal{L}_\mathrm{e}$ such that[1]

$$\left[\nabla\sigma(\zeta)\cdot\partial_\theta\zeta_0^\perp\right] = \mathcal{L}_\mathrm{i}(\xi)\left[\nabla\sigma(\zeta)\cdot\partial_\theta\zeta_0\right], \tag{7a}$$

$$\left[\nabla c^\star(\zeta)\cdot\partial_\theta\zeta_0\right] = \mathcal{L}_\mathrm{e}(\xi)\left[\nabla c^\star(\zeta)\cdot\partial_\theta\zeta_0^\perp\right]. \tag{7b}$$

[1] Observe that for $\xi = 0$, Γ is the unit circle and the relations (7) are consistent with a simple calculus in Fourier series.

These operators are defined as

$$\mathcal{L}_{\mathrm{i}}(\xi) = \mathcal{H} + \mathcal{A}_1(\xi), \tag{8a}$$

$$\mathcal{L}_{\mathrm{e}}(\xi) = \frac{1 - R_0^{-2|D|}}{1 + R_0^{-2|D|}}\mathcal{H} + \mathcal{A}_2(\xi), \tag{8b}$$

where the operators $\mathcal{A}_1$ and $\mathcal{A}_2$ belong to $L_0(2, s\,; 2)$.

Remark 8. *For $\xi \equiv 0$, Γ is the unit circle and simple calculations in Fourier series imply that the inner Dirichlet-to-Neumann and the outer Neumann-to-Dirichlet maps are nothing but $\mathcal{L}_{\mathrm{i}} = \mathcal{H}$ and $\mathcal{L}_{\mathrm{e}} = \frac{1-R_0^{-2|D|}}{1+R_0^{-2|D|}}\mathcal{H}$ respectively. The above lemma generalizes these formula to a non-circular geometry.*

Proof. The proof follows the part 4 of Iguchi's paper [6]. Define the function z and w as

$$z(\theta) = \zeta_0(\theta) + \xi(\theta), \quad \text{and} \quad w(\theta) = R_0 e^{i\theta}. \tag{9}$$

We identify $\mathbb{R}^2$ and $\mathbb{C}$. Let F_{i} and F_{e} be defined by

$$F_{\mathrm{i}}(z) = \partial_x \sigma(z) - i\partial_y \sigma(z), \quad F_{\mathrm{e}}(z) = \partial_x c^\star(z) - i\partial_y c^\star(z),$$

and define the functions of the variable θ, f_{i}, f_{e} and g_{e}, as

$$f_{\mathrm{i}}(\theta) = F_{\mathrm{i}}(z(\theta)), \quad f_{\mathrm{e}}(\theta) = F_{\mathrm{e}}(z(\theta)), \quad g_{\mathrm{e}}(\theta) = F_{\mathrm{e}}(w(\theta)).$$

First remark that

$$\Re(e^{i\theta} f_{\mathrm{i}}) = \nabla\sigma|_\zeta \cdot \partial_\theta \zeta_0^\perp, \quad \Im(e^{i\theta} f_{\mathrm{i}}) = -\nabla\sigma|_\zeta \cdot \partial_\theta \zeta_0, \tag{10a}$$

$$\Re(e^{i\theta} f_{\mathrm{e}}) = \nabla c^\star|_\zeta \cdot \partial_\theta \zeta_0^\perp, \quad \Im(e^{i\theta} f_{\mathrm{e}}) = -\nabla c^\star|_\zeta \cdot \partial_\theta \zeta_0, \tag{10b}$$

Observe also that the Dirichlet boundary condition (1c) on $c^\star$ implies that the tangent gradient of $c^\star$ vanishes on $\partial\Omega$[2]:

$$\nabla c^\star(R_0 e^{i\theta}) \cdot \begin{pmatrix} -\sin\theta \\ \cos\theta \end{pmatrix} = 0, \tag{11a}$$

hence

$$\forall \theta \in [0, 2\pi] \setminus \{\pm\pi/2\}, \quad g_{\mathrm{e}}(\theta) = \frac{e^{-i\theta}}{\cos\theta}\, \partial_x c^\star|_{R_0 e^{i\theta}}, \quad \text{and} \quad \partial_x c^\star|_{\pm i R_0} = 0. \tag{11b}$$

Since F_{i} and F_{e} are holomorphic, for any $z_0 \in \Gamma$ the Cauchy-Riemann formula implies

$$F_{\mathrm{i}}(z_0) = \frac{1}{i\pi}\text{p.v.} \int_\Gamma \frac{F_{\mathrm{i}}(z)}{z - z_0} dz,$$

$$-F_{\mathrm{e}}(z_0) = \frac{1}{i\pi}\text{p.v.} \int_\Gamma \frac{F_{\mathrm{e}}(z)}{z - z_0} dz - \frac{1}{i\pi}\int_{\partial\Omega} \frac{F_{\mathrm{e}}(w)}{w - z_0} dw,$$

[2]Note that Iguchi introduced the notation

$$W_{\mathrm{e}}^{(r)} - i W_{\mathrm{e}}^{(\theta)} = g_{\mathrm{e}}(\theta) e^{i\theta},$$

and thus equation (11) reads $W_{\mathrm{e}}^{(\theta)} = 0$. If $\partial\Omega$ is a perturbation of a circle, $\partial\Omega = \left\{R_0(1 + b(\theta))e^{i\theta},\, \theta \in \mathbb{T}\right\}$, then, due to homogeneous Dirichlet condition on $\partial\Omega$ we deduce $W_{\mathrm{e}}^{(\theta)} = \frac{b'}{1+b} W_{\mathrm{e}}^{(r)}$. In [6] homogeneous Neuman condition is imposed, which leads to $W^{(r)} = \frac{b'}{1+b} W^{(\theta)}$ as given by equation (4.2) page 534.

and for any $w_0 \in \partial\Omega$ we have

$$F_{\mathrm{e}}(w_0) = \frac{1}{i\pi}\text{p.v.}\int_{\partial\Omega}\frac{F_{\mathrm{e}}(w)}{w-w_0}dw - \frac{1}{i\pi}\int_{\Gamma}\frac{F_{\mathrm{e}}(z)}{z-w_0}dz.$$

Writing $z_0 = z(\theta)$ and $w_0 = w(\theta)$, the above integrals read respectively, for any $\theta \in \mathbb{T}$,

$$f_{\mathrm{i}}(\theta) = \frac{1}{i\pi}\text{p.v.}\int_0^{2\pi}\frac{f_{\mathrm{i}}(\varphi)}{z(\varphi)-z(\theta)}\,\frac{dz}{d\varphi}\,d\varphi, \tag{12a}$$

$$-f_{\mathrm{e}}(\theta) = \frac{1}{i\pi}\text{p.v.}\int_0^{2\pi}\frac{f_{\mathrm{e}}(\varphi)}{z(\varphi)-z(\theta)}\,\frac{dz}{d\varphi}\,d\varphi - \frac{1}{i\pi}\int_0^{2\pi}\frac{g_{\mathrm{e}}(\varphi)}{w(\varphi)-z(\theta)}\,\frac{dw}{d\varphi}\,d\varphi, \tag{12b}$$

$$g_{\mathrm{e}}(\theta) = \frac{1}{i\pi}\text{p.v.}\int_0^{2\pi}\frac{g_{\mathrm{e}}(\varphi)}{w(\varphi)-w(\theta)}\,\frac{dw}{d\varphi}\,d\varphi - \frac{1}{i\pi}\int_0^{2\pi}\frac{f_{\mathrm{e}}(\varphi)}{z(\varphi)-w(\theta)}\,\frac{dz}{d\varphi}\,d\varphi, \tag{12c}$$

According to (9), since $\zeta_0(\theta) = e^{i\theta}$, one has

$$\frac{1}{z(\varphi)-z(\theta)}\frac{dz(\varphi)}{d\varphi} = \frac{ie^{i\varphi}}{e^{i\varphi}-e^{i\theta}} + \frac{\partial}{\partial\varphi}\log\left(\frac{e^{i\varphi}-e^{i\theta}+\xi(\varphi)-\xi(\theta)}{e^{i\varphi}-e^{i\theta}}\right),$$
$$\frac{1}{w(\varphi)-z(\theta)}\frac{dw(\varphi)}{d\varphi} = \frac{ie^{i\varphi}}{e^{i\varphi}-R_0^{-1}e^{i\theta}} + \frac{\partial}{\partial\varphi}\log\left(\frac{R_0e^{i\varphi}-e^{i\theta}-\xi(\theta)}{R_0e^{i\varphi}-e^{i\theta}}\right),$$
$$\frac{1}{z(\varphi)-w(\theta)}\frac{dz(\varphi)}{d\varphi} = \frac{ie^{i\varphi}}{e^{i\varphi}-R_0e^{i\theta}} + \frac{\partial}{\partial\varphi}\log\left(\frac{e^{i\varphi}+\xi(\varphi)-R_0e^{i\varphi}}{e^{i\varphi}-R_0e^{i\theta}}\right),$$

and obviously,

$$\frac{1}{w(\varphi)-w(\theta)}\frac{dw(\varphi)}{d\varphi} = \frac{ie^{i\varphi}}{e^{i\varphi}-e^{i\theta}}.$$

Note that the above decompositions are useful since for small ξ, the second terms of the right-hand sides are small, and thus the leading parts are driven by the first terms independent of ξ. Moreover, as mentioned by Iguchi, one has the following characterization of the leading integral operators, for any $f \in L^2(\mathbb{T})$:

$$\frac{1}{i\pi}\text{p.v.}\int_0^{2\pi}\frac{ie^{i\varphi}}{e^{i\varphi}-e^{i\theta}}f(\varphi)\,d\varphi = e^{-i\theta}(i\mathcal{H}-\mathcal{P}_0)[e^{i\theta}f], \tag{13}$$

$$\frac{1}{i\pi}\int_0^{2\pi}\frac{ie^{i\varphi}}{e^{i\varphi}-R_0^{-1}e^{i\theta}}f(\varphi)\,d\varphi = e^{-i\theta}\left(i\mathcal{H}R_0^{-|D|+1} + (R_0^{-|D|+1}-R_0\mathcal{P}_0)\right)[e^{i\theta}f], \tag{14}$$

$$\frac{1}{i\pi}\int_0^{2\pi}\frac{ie^{i\varphi}}{e^{i\varphi}-R_0e^{i\theta}}f(\varphi)\,d\varphi = e^{-i\theta}\left(i\mathcal{H}R_0^{-|D|-1} - (R_0^{-|D|-1}+R_0^{-1}\mathcal{P}_0)\right)[e^{i\theta}f]. \tag{15}$$

To simplify the notations, we set

$$\mathcal{J}_0 = i\mathcal{H}-\mathcal{P}_0, \tag{16a}$$

$$\mathcal{K}_0 = i\mathcal{H}R_0^{-|D|+1} + (R_0^{-|D|+1}-R_0\mathcal{P}_0) = \mathcal{K}_0^{\Re} + i\mathcal{K}_0^{\Im}, \tag{16b}$$

$$\mathcal{L}_0 = i\mathcal{H}R_0^{-|D|-1} - (R_0^{-|D|-1}+R_0^{-1}\mathcal{P}_0) = \mathcal{L}_0^{\Re} + i\mathcal{L}_0^{\Im}. \tag{16c}$$

We also introduce the 3 integral operators with complex symbols:

$$\mathcal{B}_j(\xi)f(\theta) = -\frac{1}{\pi}\int_0^{2\pi} b_j(\varphi,\theta;\xi)\partial_\varphi f(\varphi)\,d\varphi,$$

where b_j are the complex-valued functions defined as

$$b_1(\varphi,\theta;\xi) = \log\left(\frac{e^{i\varphi}-e^{i\theta}+\xi(\varphi)-\xi(\theta)}{e^{i\varphi}-e^{i\theta}}\right), \tag{17}$$

$$b_2(\varphi,\theta;\xi) = \log\left(\frac{R_0e^{i\varphi}-e^{i\theta}-\xi(\theta)}{R_0e^{i\varphi}-e^{i\theta}}\right), \tag{18}$$

$$b_3(\varphi,\theta;\xi) = \log\left(\frac{e^{i\varphi}+\xi(\varphi)-R_0e^{i\varphi}}{e^{i\varphi}-R_0e^{i\theta}}\right). \tag{19}$$

Thanks to these operators, equalities (12) read now

$$f_{\rm i}(\theta) = e^{-i\theta}\mathcal{J}_0[e^{i\theta}f_{\rm i}] + (\mathcal{B}_1(\xi)f_{\rm i})(\theta), \tag{20a}$$

$$-f_{\rm e}(\theta) = e^{-i\theta}\mathcal{J}_0[e^{i\theta}f_{\rm e}] - e^{-i\theta}\mathcal{K}_0[e^{i\theta}g_{\rm e}] + (\mathcal{B}_1(\xi)f_{\rm e})(\theta) - (\mathcal{B}_2(\xi)g_{\rm e})(\theta), \tag{20b}$$

$$g_{\rm e}(\theta) = e^{-i\theta}\mathcal{J}_0[e^{i\theta}g_{\rm e}] - e^{-i\theta}\mathcal{L}_0[e^{i\theta}f_{\rm e}] + (\mathcal{B}_1(\xi)g_{\rm e})(\theta) - (\mathcal{B}_3(\xi)f_{\rm e})(\theta). \tag{20c}$$

It is crucial noting that thanks to classical Sobolev embedding, and similarly to Lemma 5.11 page 549 of Iguchi's paper [6], for $k\in\{1,2,3\}$, the above operator $\mathcal{B}_k$ belongs to $L_0(2,s\,;2)$, for $s\geq 3$, which means that they satisfy (6) with $r=2$, $\tau=2$, for any $s\geq 3$.

According to (6) the norm of $\mathcal{B}_1(\xi)$ as an operator on $H^2(\mathbb{T})$ is bounded by the norm of ξ in $H^s(\mathbb{T})$. Therefore for ξ small enough in H^s the norm of $\Re(e^{i\theta}\mathcal{B}_1(\xi)e^{-i\theta})$ is also small, bounded by $\|\xi\|_{H^s}$ and thus the operator $1+\mathcal{P}_0-\Re(e^{i\theta}\mathcal{B}_1(\xi)e^{-i\theta})$ is a perturbation of $1+\mathcal{P}_0$ which is invertible. Thus $1+\mathcal{P}_0-\Re(e^{i\theta}\mathcal{B}_1(\xi)e^{-i\theta})$ is also invertible and one has

$$\left(1+\mathcal{P}_0-\Re(e^{i\theta}\mathcal{B}_1(\xi)e^{-i\theta})\right)^{-1} - \left(1-\frac{1}{2}\mathcal{P}_0\right) \in L_0(2,s\,;2), \quad \text{for any } s\geq 3.$$

Denote by

$$\mathcal{J}(\xi) = \mathcal{J}_0 + e^{i\theta}\mathcal{B}_1(\xi)e^{-i\theta}, \tag{21}$$

$$\mathcal{K}(\xi) = \mathcal{K}_0 + e^{i\theta}\mathcal{B}_2(\xi)e^{-i\theta}, \tag{22}$$

$$\mathcal{L}(\xi) = \mathcal{L}_0 + e^{i\theta}\mathcal{B}_3(\xi)e^{-i\theta}, \tag{23}$$

and define, for $n=1,2,3$ the real integral operators $\mathcal{A}_n^{\Re}(\xi)$ and $\mathcal{A}_n^{\Im}(\xi)$ by

$$\mathcal{A}_n^{\Re}(\xi) + i\mathcal{A}_n^{\Im}(\xi) = e^{i\theta}\mathcal{B}_n(\xi)e^{-i\theta}.$$

Noting that thanks to equality (11), $e^{i\theta}g_{\rm e}$ is a real-valued function, multiplying (20c) by $e^{i\theta}$ and taking successively the real and the imaginary parts, we infer the relations between $g_{\rm e}$ and $f_{\rm e}$:

$$\begin{aligned}(1+\mathcal{P}_0-\mathcal{A}_1^{\Re})e^{i\theta}g_{\rm e} = &-\left(\mathcal{H}R^{-|D|-1}+\mathcal{A}_3^{\Im}\right)\nabla c\cdot\partial_\theta\zeta_0\\ &+\left(R_0^{-|D|-1}+R_0^{-1}\mathcal{P}_0+\mathcal{A}_3^{\Re}\right)\nabla c\cdot\partial_\theta\zeta_0^{\perp},\end{aligned} \tag{24a}$$

$$\begin{aligned}\left(\mathcal{H}+\mathcal{A}_1^{\Im}\right)e^{i\theta}g_{\rm e} = &\left(\mathcal{H}R^{-|D|-1}+\mathcal{A}_3^{\Im}\right)\nabla c\cdot\partial_\theta\zeta_0^{\perp}\\ &+\left(R_0^{-|D|-1}+R_0^{-1}\mathcal{P}_0+\mathcal{A}_3^{\Re}\right)\nabla c\cdot\partial_\theta\zeta_0.\end{aligned} \tag{24b}$$

Thus we obtain

$$e^{i\theta} f_{\mathrm{i}}(\theta) = \mathcal{J}(\xi)[e^{i\theta} f_{\mathrm{i}}](\theta), \tag{25}$$

$$-e^{i\theta} f_{\mathrm{e}}(\theta) = \mathcal{J}(\xi)[e^{i\theta} f_{\mathrm{e}}](\theta) + \mathcal{K}(\xi)\Big\{1 - \Re\left(\mathcal{J}(\xi)\right)\Big\}^{-1}\left[\Re\Big(\mathcal{L}(\xi)[e^{i\theta} f_{\mathrm{e}}]\Big)\right]. \tag{26}$$

Taking the real part of (25), using (10) leads to

$$\left(1 + \mathcal{P}_0 - \mathcal{A}_1^{\Re}(\xi)\right)\left[\nabla\sigma(\zeta)\cdot\partial_\theta\zeta_0^\perp\right] = \left(\mathcal{H} + \mathcal{A}_1^{\Im}(\xi)\right)\left[\nabla\sigma(\zeta)\cdot\partial_\theta\zeta_0\right], \tag{27}$$

from which we infer (7a) by setting

$$\mathcal{L}_{\mathrm{i}}(\xi) = \left(1 + \mathcal{P}_0 - \mathcal{A}_1^{\Re}(\xi)\right)^{-1}\left(\mathcal{H} + \mathcal{A}_1^{\Im}(\xi)\right) = \mathcal{H} + \mathcal{A}_1(\xi).$$

Similarly, using the definition of $\mathcal{K}_0$ and $\mathcal{L}_0$ and observing that

$$\mathcal{H}\mathcal{P}_0 = \mathcal{P}_0\mathcal{H} = 0, \quad \mathcal{H}R_0^{-|D|} = R_0^{-|D|}\mathcal{H},$$

by taking the imaginary part of (26) and using (24), we infer that there exists $\mathcal{A}_2(\xi)$ such that

$$\nabla c^\star|_\zeta\cdot\partial_\theta\zeta_0 = \left(\frac{1 - R_0^{-2|D|}}{1 + R_0^{-2|D|}}\mathcal{H} + \mathcal{A}_2(\xi)\right)\nabla c^\star|_\zeta\cdot\partial_\theta\zeta_0^\perp.$$

It is clear that as the operators $\mathcal{B}_k$, for $k = 1, 2, 3$, the real-valued operators $\mathcal{A}_1$ and $\mathcal{A}_2$ belong to $L_0(2, s\,; 2)$, which ends the proof of Lemma 7. □

Remark 9. *Note that taking the imaginary part of* (25)*, using* (10) *leads to*

$$\left(1 + \mathcal{P}_0 - \mathcal{A}_1^{\Re}(\xi)\right)\left[\nabla\sigma(\zeta)\cdot\partial_\theta\zeta_0\right] = -\left(\mathcal{H} + \mathcal{A}_1^{\Im}(\xi)\right)\left[\nabla\sigma(\zeta)\cdot\partial_\theta\zeta_0^\perp\right]. \tag{28}$$

Remark 10. *Using the fact that* $\partial_t\zeta = \partial_t\xi$*, equation* (1a) *and the above lemma imply that*

$$\partial_t\xi\cdot\partial_\theta\zeta_0^\perp = \mathcal{L}_{\mathrm{i}}(\xi)\left\{\partial_t\xi\cdot\partial_\theta\zeta_0\right\}.$$

We now rewrite the nonlinear system(1) in terms of X_1 and X_2 defined as

$$X_1 = \xi\cdot\partial_\theta\zeta_0^\perp, \quad X_2 = \xi\cdot\partial_\theta\zeta_0.$$

Using this change of variables, the following equalities hold

$$\partial_t\xi = \partial_t X_2\partial_\theta\zeta_0 + \partial_t X_1\partial_\theta\zeta_0^\perp, \tag{29a}$$

$$\partial_\theta\xi = \left(\partial_\theta X_2 + X_1\right)\partial_\theta\zeta_0 + \left(\partial_\theta X_1 - X_2\right)\partial_\theta\zeta_0^\perp, \tag{29b}$$

$$\partial_\theta\xi^\perp = -\left(\partial_\theta X_1 - X_2\right)\partial_\theta\zeta_0 + \left(\partial_\theta X_2 + X_1\right)\partial_\theta\zeta_0^\perp. \tag{29c}$$

Since $\partial_\theta\zeta = \partial_\theta\zeta_0 + \partial_\theta\xi$, we show in the next lemma that the system can be rewritten in terms of X_1, X_2 and their derivatives.

Lemma 11 (Equivalent problems)**.** *Problem* (1) *is equivalent to the following nonlinear problem written in terms of* (X_1, X_2)*:*

$$\partial_t X_1 = \mathcal{L}_{\mathrm{i}}(\xi)\left\{\partial_t X_2\right\}, \tag{30}$$

$$\begin{aligned}&\frac{\partial_t\zeta\cdot\partial_\theta\zeta}{|\partial_\theta\zeta|^2}(1 + X_1 + \partial_\theta X_2) + \frac{g}{|\partial_\theta\zeta|}\left(\partial_\theta X_1 - X_2\right)\\ &= \mathcal{L}_{\mathrm{e}}(\xi)\left\{\frac{\partial_t\zeta\cdot\partial_\theta\zeta}{|\partial_\theta\zeta|^2}(\partial_\theta X_1 - X_2) - \frac{g}{|\partial_\theta\zeta|}(1 + X_1 + \partial_\theta X_2)\right\},\end{aligned} \tag{31}$$

where

$$|\partial_\theta \zeta| = \sqrt{(1+\partial_\theta X_2 + X_1)^2 + (\partial_\theta X_1 - X_2)^2}, \tag{32}$$
$$\partial_t \zeta \cdot \partial_\theta \zeta = \partial_t X_2 (1 + \partial_\theta X_2 + X_1) + \partial_t X_1 \left(\partial_\theta X_1 - X_2\right). \tag{33}$$

Remark 12. *We thus have reduced our free boundary problem to the equivalent nonlinear system* (30)–(31) *on* (X_1, X_2) *set in the domain* $(0,T)\times\mathbb{T}$. *The well-posedness of this equivalent problem will thus lead to the well-posedness of our free boundary problem. The advantage lies in the fact that the involved operators are now better understood thanks to Lemma 7.*

Proof. Equality (30) comes from Lemma 7 and Remark 10. Differentiating (1e) with respect to θ, we have

$$\partial_\theta \zeta(t,\theta) \cdot \nabla \sigma(t, \zeta(t,\theta)) = \partial_\theta \zeta \cdot \nabla c^\star(\zeta),$$

and thus thanks to (1a) we deduce:

$$\partial_\theta \zeta \cdot \partial_t \zeta = \partial_\theta \zeta \cdot \nabla c^\star(\zeta).$$

The second equality of (1c) reads then

$$(\partial_\theta \zeta)^\perp \cdot \nabla c^\star = -|\partial_\theta \zeta| g(t, \zeta(t,\theta)).$$

Therefore we obtain the following expression of $\nabla c^\star(\zeta)$:

$$\nabla c^\star(\zeta) = \frac{1}{|\partial_\theta \zeta|^2} \left((\partial_t \zeta \cdot \partial_\theta \zeta) \partial_\theta \zeta - g |\partial_\theta \zeta| \partial_\theta \zeta^\perp \right).$$

Thanks to (7b) and using the equalities (29) we deduce equation (31). □

2.1 Quasilinearization

Following [6], we quasilinearize the system (30)–(31). Let $\mathbb{Y} = (Y_i)_{i=1,4}$ be defined by

$$Y_1 = X_1, \quad Y_2 = X_2, \quad Y_3 = \partial_\theta X_1 - X_2, \quad Y_4 = \partial_\theta X_2 + X_1,$$

and set

$$W = \partial_t X_2.$$

From (30), we get

$$\partial_t Y_1 = \mathcal{L}_{\rm i}(\mathbb{Y})\{W\}, \tag{34a}$$
$$\partial_t Y_2 = W, \tag{34b}$$
$$\partial_t Y_3 = \partial_\theta \mathcal{L}_{\rm i}(\mathbb{Y})\{W\} - W, \tag{34c}$$
$$\partial_t Y_4 = \partial_\theta W + \mathcal{L}_{\rm i}(\mathbb{Y})\{W\}. \tag{34d}$$

The following lemma is straightforward.

Lemma 13. *Let* $s \geq 3$. *Suppose that* $W \in L^2(0,T;H^{s+1})$ *and let* $\mathbb{Y}_0 \in (H^s(\mathbb{T}))^4$. *Then the solution* $\mathbb{Y}$ *to* (34) *with the initial condition* $\mathbb{Y}|_{t=0} = \mathbb{Y}_0$ *is such that*

$$\mathbb{Y} \in L^\infty(0,T;(H^s(\mathbb{T}))^4),$$

and

$$\|\mathbb{Y}\|_{L^\infty(0,T;(H^s(\mathbb{T}))^4)} \leq \|\mathbb{Y}_0\|_{(H^s(\mathbb{T}))^4} + C\sqrt{T}\|W\|_{L^2(0,T;H^{s+1}(\mathbb{T}))}.$$

Moreover, if $(W_1, W_2) \in \left(L^2(0,T;H^{s+1})\right)^2$ *and* $\mathbb{Y}_0 \in (H^s(\mathbb{T}))^4$, *then the corresponding solutions* $\mathbb{Y}_1$ *and* $\mathbb{Y}_2$ *satisfy:*

$$\|\mathbb{Y}_1 - \mathbb{Y}_2\|_{L^\infty(0,T;(H^s(\mathbb{T}))^4)} \leq C\sqrt{T}\|W_1 - W_2\|_{L^2(0,T;H^{s+1}(\mathbb{T}))}.$$

It remains to obtain the nonlinear equation for W. Equation (31) reads now

$$\begin{aligned} &F_1^2(\mathbb{Y})W + F_1(\mathbb{Y})F_2(\mathbb{Y})\,\mathcal{L}_{\rm i}(\mathbb{Y})\{W\} + F_2(\mathbb{Y})g(t,\zeta(t,\theta) \\ &= \mathcal{L}_{\rm e}(\mathbb{Y})\left\{F_1(\mathbb{Y})F_2(\mathbb{Y})W + F_1^2(\mathbb{Y})\,\mathcal{L}_{\rm i}(\mathbb{Y})W - F_1(\mathbb{Y})g(t,\zeta(t,\theta)\right\}, \end{aligned} \tag{35}$$

where F_i are given for $i = 1, 2$ by

$$F_1(\mathbb{Y}) = \frac{1+Y_4}{\sqrt{(1+Y_4)^2+Y_3^2}}, \quad F_2(\mathbb{Y}) = \frac{Y_3}{\sqrt{(1+Y_4)^2+Y_3^2}}.$$

Similarly to Yosihara's and Iguchi's papers, differentiating the above equation with respect to t, we infer the following equation for W:

$$\partial_t W + 2g\frac{1}{1+R_0^{-2|D|}}\mathcal{H}\partial_\theta W = f(g, \partial_t g, \mathbb{Y}, W, \partial_\theta W), \tag{36}$$

where f is such that there exists $C > 0$ such that if $\mathbb{Y}$ and g are small enough in $(L^\infty(0,T;H^s(\mathbb{T})))^4$, $W^{1,\infty}(0,T;H^{s+1/2}(\Omega))$ respectively, one has the following inequalities for any W small enough in $L^\infty(0,T;H^s) \cap L^2(0,T;H^{s+1})$:

$$\begin{aligned} \|f(\cdots, \mathbb{Y}, W, \partial_\theta W)\|_{L^2(0,T;H^s)} \leq C\Big(&\sqrt{T}\|W\|_{L^\infty(0,T;H^s)} \\ &+\|\mathbb{Y}\|_{(L^\infty(0,T;H^s))^4}\|W\|_{L^2(0,T;H^{s+1})}\Big), \end{aligned} \tag{37}$$

$$\begin{aligned} \|f(\cdots, W_1, \partial_\theta W_1) - f(\cdots, \mathbb{Y}, W_2, \partial_\theta W_2)\|_{L^2(0,T;H^s)} \leq C\Big(&\sqrt{T}\|W_1 - W_2\|_{L^\infty(0,T;H^s)} \\ &+\|\mathbb{Y}\|_{(L^\infty(0,T;H^s))^4}\|W_1 - W_2\|_{L^2(0,T;H^{s+1})}\Big), \end{aligned} \tag{38}$$

where the dots $\cdots$ hold for the variables $(g, \partial_t g, \mathbb{Y})$. For the sake of conciseness, we do not make explicit the expression of f in terms of F_1 and F_2, but as in Yosihara's and Iguchi's papers, this function has clearly the above properties.

The main difference with these works lies in the partial differential equation satisfied by $W := \partial_t X_2$. Actually, neglecting the non-linear terms of (36) we observe that the equation is parabolic since the symbol of $\mathcal{H}\partial_\theta$ is

$$\mathfrak{s}_{\mathcal{H}\partial_\theta}(k) = |k|, \quad k \in \mathbb{Z}.$$

Moreover one can easily check that due to the hypotheses (4) on g at Theorem 3 that we recall here:

$$\begin{aligned} &g \in W^{1,\infty}(\mathbb{R}^+; H^{s+1/2}(\Omega)), \qquad \|g\|_{W^{1,\infty}(\mathbb{R}^+;H^{s+1/2}(\Omega))} \leq M, \quad \text{for a given } M > 0, \\ &\forall (t,x) \in \mathbb{R}\times\Omega, \quad g(t,x) \geq \alpha, \quad \text{for a given } \alpha > 0, \end{aligned}$$

the time-dependent operator $(\mathcal{A}_g, H^1)$ defined as

$$\mathcal{A}_g \,:\, (t,w) \in \mathbb{R}^+ \times H^1 \mapsto 2g(t)\frac{1}{1+R_0^{-2|D|}}\mathcal{H}\partial_\theta w,$$

is m-accretive in the sense of Kato [8] since it satisfies the following properties:

1. $D(\mathcal{A}_g) = \{u \in H^{1/2} : \quad \mathcal{H}\partial_\theta u \in L^2\} \subset L^2$ does not depend on the time t.
2. For almost any $t > 0$, $(\mathcal{A}_g(t), H^1)$ is m-accretive. This easily comes from the fact that $\langle \mathcal{H}\partial_\theta w, w\rangle = \|w - \int_{\mathbb{T}} w\|^2_{H^{1/2}}$, therefore for any $\lambda > 0$, one has

$$\|v + \lambda \mathcal{A}_g(t)v\|^2_{L^2} \geq \|v\|^2_{L^2} + 4\alpha \left\|v - \int_{\mathbb{T}} v\right\|^2_{H^{1/2}} + 4\alpha^2 \|\partial_\theta v\|^2_{L^2} \geq \|v\|^2_{L^2}.$$

   Moreover for any $\lambda > 0$, for any $f \in L^2$, the equation

$$u + \lambda \mathcal{A}_g(t)u = f,$$

   has a unique solution since the bilinear form

$$a(u,v) := \int_{\mathbb{T}} uv d\theta + \lambda \int_{\mathbb{T}} \mathcal{A}_g(t)u\, v d\theta,$$

   is continuous and coercive on $H^{1/2}$ thanks to (4), and thus Lax-Milgram lemma provides the existence and uniqueness of u in $D(\mathcal{A}_g)$.
3. Finally, for almost any $(t,s) \in (\mathbb{R}^+)^2$ one has

$$\mathcal{A}_g(t)v - \mathcal{A}_g(s)v = (g(t) - g(s))\frac{2}{1+R_0^{-2|D|}}\mathcal{H}\partial_\theta v,$$

   and thus once again thanks to (4), one has

$$\|\mathcal{A}_g(t)v - \mathcal{A}_g(s)v\|_{L^2} \leq \frac{\|g\|_{W^{1,\infty}(\mathbb{R}^+;H^{s+1/2})}}{\alpha}|t-s|(1 + \|v\| + \|\mathcal{A}_g(s)v\|).$$

Therefore the 3 conditions of Kato's paper [8] are satisfied and thus the time-dependent equation $\partial_t w + \mathcal{A}_g(t)(w) = f$ admits a unique solution for any $f \in L^1(0,T;H^{1/2})$.

In the following, we focus on the energy estimates in order to prove the well-posedness of the quasilinearized system, thanks to the use of a classical fixed point method.

Lemma 14 (*A priori* energy estimates)**.** *Let $s \geq 3$ and $\alpha > 0$. Suppose that there exists a 2π–periodic solution $W \in L^\infty(0,T;H^{s+1/2}) \cap L^2(0,T;H^{s+1})$ satisfying equation* (36) *with the initial condition $W|_{t=0} = W_0$. Then there exist $M > 0$ and $T > 0$ small enough such that if $W_0 \in H^s(\mathbb{T})$ and if $\mathbb{Y}$ and g satisfy*

$$\|W_0\|_{H^s} \leq M, \quad \|\mathbb{Y}\|_{L^\infty(0,T;H^s)} \leq M,$$
$$g \in W^{1,\infty}(0,T;H^{s+1/2}) : \, g(t,x) \geq \alpha, \, \forall (t,x) \in (0,T)\times\Omega,$$

then the solution W satisfies:

$$\sup_{t\in(0,T)} \|W(t,\cdot)\|_{H^{s+1/2}} + \|W\|_{L^2(0,T;H^{s+1})} \leq M.$$

Proof. The proof is standard, thanks to the embedding $H^s \hookrightarrow L^\infty$ for any $s > 1/2$ and using the fact that

$$\langle W, \mathcal{H}\partial_\theta W\rangle = \|W - \bar{W}\|^2_{H^{1/2}}.$$

More precisely, multiplying first equation (36) by W and integrating by part in the space variable lead to

$$\begin{aligned}\frac{1}{2}\frac{d}{dt}\|W\|^2_{L^2} + \alpha\|W-\bar{W}\|^2_{H^{1/2}} &\leq \frac{d}{dt}\|W\|^2_{L^2} + \int_{\mathbb{T}} g\frac{1}{1+R_0^{-2|D|}}W\mathcal{H}\partial_\theta W\, d\theta,\\ &\leq \int_{\mathbb{T}} |fW| d\theta,\end{aligned}$$

from which we infer that for M and T small enough,

$$\sup_{t\in(0,T)}\|W(t,\cdot)\|_{L^2} \leq M, \quad \|W\|_{L^2(0,T;H^{1/2})} \leq M.$$

Similarly, multiplying by $\mathcal{H}\partial_\theta W$ we infer that for M small enough:

$$\frac{1}{2}\frac{d}{dt}\|W-\bar{W}\|^2_{H^{1/2}} + \frac{1}{2}\alpha\|W-\bar{W}\|^2_{H^1} \leq \int |f\mathcal{H}\partial_\theta W| d\theta,$$

and thus we infer that for M and T small enough,

$$\sup_{t\in(0,T)}\|W(t,\cdot)\|_{H^{1/2}} \leq M, \quad \|W\|_{L^2(0,T;H^1)} \leq M.$$

Deriving until the order s the equation (36) with respect to θ, and denoting by $Z := \partial^s_\theta W$ we obtain

$$\partial_t Z + 2g\frac{1}{1+R_0^{-2|D|}}\mathcal{H}\partial_\theta Z = G,$$

where the right hand side is in $L^2(0,T;L^2)$ according to (37). The estimations

$$\begin{aligned}\int_0^T\int_{\mathbb{T}} |GZ| d\theta\, dt &\leq \|G\|_{L^2(0,T;L2)}\|Z\|_{L^2(0,T;L^2)},\\ &\leq (M+\sqrt{T})\|Z\|^2_{L^2(0,T;H^1)},\end{aligned}$$

and

$$\begin{aligned}\int_0^T\int_{\mathbb{T}} |G\mathcal{H}\partial_\theta Z| d\theta\, dt &\leq \|G\|_{L^2(0,T;L^2)}\|Z\|_{L^2(0,T;H^1)},\\ &\leq (M+\sqrt{T})\|Z\|^2_{L^2(0,T;H^1)},\end{aligned}$$

imply that for M and T small enough,

$$\sup_{t\in(0,T)}\|Z(t,\cdot)\|_{H^{1/2}} \leq M, \quad \|Z\|_{L^2(0,T;H^1)} \leq M,$$

which ends the proof. □

The contraction estimates are obtained in the similar manner.

Definition 15. *Let $M > 0$.*
We denote by $\mathcal{V}_M$ the subspace of $L^\infty(0,T;H^{s+1/2}) \cap L^2(0,T;H^{s+1})$ defined by

$$\mathcal{V}_M = \left\{ \begin{array}{l} u \in L^\infty(0,T;H^{s+1/2}) \cap L^2(0,T;H^{s+1}) \ : \\ \sup\limits_{t\in(0,T)} \|u(t,\cdot)\|_{H^{s+1/2}} \leq M, \quad \|u\|_{L^2(0,T;H^{s+1})} \leq M \end{array} \right\}.$$

For the sake of conciseness, we leave the proof of the following lemma to the reader, since it is very similar to the above *a priori* estimates.

Lemma 16. *Let Φ be the mapping from $L^\infty(0,T;H^{s+1/2}) \cap L^2(0,T;H^{s+1})$ into itself defined by $\Phi(U) := W$, where W is the solution to*

$$\partial_t W + 2g \frac{1}{1+R_0^{-2|D|}} \mathcal{H} \partial_\theta W = f(g, \partial_t g, \mathbb{Y}, U, \partial_\theta U). \tag{39}$$

There exist M and T small enough such that Φ is a continuous and contracting mapping from $\mathcal{V}_M$ into itself.

Using the above lemmas 13–14–16 leads straightforwardly to the following theorem, thanks to a classical application of the fixed point theorem.

Theorem 17. *Let $s \geq 3$. Let $g \in W^{1,\infty}(0,T;H^{s+1/2}(\Omega))$, such that*

$$\forall (t,x) \in (0,T) \times \Omega, \quad g(t,x) \geq \alpha > 0.$$

There exists $M > 0$ and $T > 0$ small enough such that for $\mathbb{Y}_0 \in (H^s(\mathbb{T}))^4$ and $W_0 \in H^{s+1/2}(\mathbb{T})$ satisfying

$$\|Y_0\|_{H^s} \leq M, \quad \|W_0\|_{H^{s+1/2}} \leq M.$$

Then, the quasilinearized problem (34)–(36) with the initial condition $(\mathbb{Y}, W)|_{t=0} = (\mathbb{Y}_0, W_0)$ admits a unique solution $(\mathbb{Y}, W)$ such that

$$\mathbb{Y} \in L^\infty(0,T;H^s), \quad W \in \mathcal{V}_M. \tag{40}$$

In order to obtain the well-posedness of the initial free boundary problem, it remains to show that (Y_1, Y_2) are effectively the (X_1, X_2) solutions to problem (30)–(31). This is quite obvious since the first two equations of (34) imply that (30) is satisfied. Moreover, at the initial time W satisfies equation (35) and by construction of the equation for $\partial_t W$ this equality is propagated at any time. Since we clearly have $W = \partial_t Y_2$, $Y_3 = \partial_\theta Y_1 - Y_2$ and $Y_3 = \partial_\theta Y_2 + Y_1$, we infer that Y_1 and Y_2 satisfy (30)–(31).

3 Numerical methods and simulations

In this section, we describe the first-order 2D-Cartesian method used to solve Problem (1) in the Eulerian form, meaning that (1a) is replaced by (2). It is based on level set [15] and finite-difference methods on Cartesian grids. The discretized differential operators are derived from centered stencils, on each subdomain delimited by the interface, using the ghost-fluid method [3, 5]. The static subproblems (1b)-(1c) and (1d)-(1e) are approximated by methods with second order of accuracy, which is the natural choice for Poisson's problems. Nevertheless, the overall method is first order accurate due to the complex coupling. It is presented as follows:

- Poisson-Neumann problem (1b)-(1c) in the exterior area (*ligands*),

- Poisson-Dirichlet problem (1d)-(1e) in the interior area (*signal*),
- Extension of the velocity for the transport of the level set function (1a).

We first give the different numerical schemes used to solve each subproblem, and then we provide some convergence results, with observations about the relevance of Hypothesis (4). Finally, some numerical simulations are presented with a source satisfying Hypothesis (4), that make appear the invadopodia or pseudopodia-like protrusion formations.

Notation 18. *The Cartesian grid is the natural choice to avoid remeshing at each iteration, as the interface evolves, in particular for parallelization purposes.*

- *The space steps δx and δy are denoted by h and such that*

$$h = \delta x = \delta y.$$

  Thus, an accuracy of order p in space must be interpreted as an accuracy at the rate p, like $\mathcal{O}(h^p)$.

- *The time step is denoted by δt and the time discretization is defined by*

$$t^n = n\,\delta t.$$

- *The discretized differential operators are denoted by Δ^h, ∇^h and $\partial^h_{\mathbf{n}^h}$ for the Laplacian operator Δ, the gradient ∇ and the normal derivative $\partial_{\mathbf{n}}$, respectively.*
- *Throughout the paper, the following notations are used:*
  - *The grid nodes are denoted by $x_{i,j}$,*
  - *$\varphi^n_{i,j}$ denotes the approximation at the point $(t^n, x_{i,j})$ of any function φ defined on Ω,*
  - *Ω^h denotes the set of grid nodes,*
  - *$\mathcal{O}^{e,h}_{t^n}$ and $\mathcal{O}^{i,h}_{t^n}$ stand for the sets of grid nodes $(t^n, x_{i,j})$ where $\psi^n_{i,j} > 0$ and $\psi^n_{i,j} < 0$, respectively.*
  - *c^h, σ^h, ψ^h and $\mathbf{n}^h$ are the numerical approximations of $c^\star$, σ, ψ and $\mathbf{n}$,*
  - *$\Gamma^h_{t^n}$ is the set of the intersections of the grid axes and the level 0 of the numerical level set function ψ^h at the time t^n,*
  - *When j (and n) does not play a role in the numerical stencils, we write φ_i and x_i instead of $\varphi^n_{i,j}$ and $x_{i,j}$ to lighten the formulas.*

3.1 Static subproblems

We first present the numerical methods used to tackle the static problems (1b)-(1c) and (1d)-(1e).

3.1.1 Exterior static problem (1b)-(1c) with a Neumann boundary condition.

In order to discretize the equation (1b) and handle the Neumann condition (1c) for the exterior problem, that stands for the ligand diffusion, we propose a Cartesian approach strongly inspired by Cisternino and Weynans in [2]. The Laplace operator is discretized thanks to the well-known Shortley-Weller scheme [20] that is consistent of order 1 near the interface and of order 2 at the other grid points (*regular points*). This scheme can be built near the interface thanks to the ghost fluid method (see Fedkiw *et al.* [3] for more details), computing the ghost values with

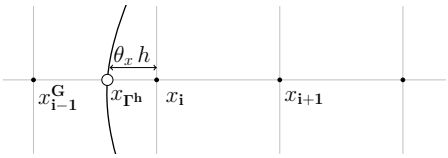

Figure 7: Ghost-Fluid method for the points near the interface.

quadratic extrapolations. For instance, the scheme for the second x-derivative is given by (as mentionned before, j is omitted)

$$\partial^h_{xx} c^h_i = \frac{c^h_{i+1} - 2\, c^h_i + c^h_{i-1}}{h^2}, \qquad \text{at the regular points of } \mathcal{O}^{e,h}, \tag{41}$$

$$\partial^h_{xx} c^h_i = \frac{2}{\theta_x\,(1+\theta_x)\,h^2}\, c_{\Gamma^h} - \frac{2}{\theta_x h^2}\, c^h_i + \frac{2}{(1+\theta_x)\,h^2}\, c^h_{i+1}, \qquad \text{in } \mathcal{O}^{e,h}, \text{ near } \Gamma, \tag{42}$$

where $\theta_x h$ denotes the distance of the point x_i to the numerical interface Γ^h in the x-axis direction (see Figure 7). If the case $\theta_x = 1$ occurs, we have $c_{\Gamma^h} = c^h_{i-1}$. The scheme (42) is then equivalent to the standard 3-point stencil scheme (41). Conversely, if $\theta_x = 0$, the point x_i is an interface point and does not belong to $\mathcal{O}^{e,h}$.

The main difficulty of the method lies in the computation of the interface values c_{Γ^h}, from the Neumann condition. The flux condition at the interface is discretized by evaluating the derivatives of c^h on Γ^h, where ∇^h is not defined. We therefore introduce new operators $\partial_x^{\Gamma^h}$ and $\partial_y^{\Gamma^h}$, that are directly or indirectly computed from other grid points, depending on whether the interface point belongs to the x-axis or to the y-axis. The key point lies in the *stencil continuity* that avoids introducing new unknowns on the interface. In Fig. 8, the point A is on the y-axis

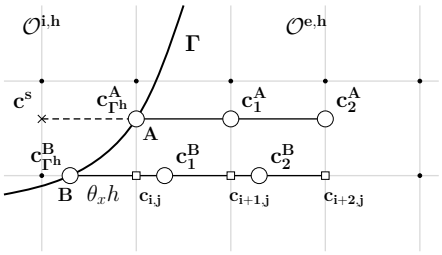

Figure 8: Interface derivative.

and the *indirect* x-derivative $\partial_x^{\Gamma^h} c^A_{\Gamma^h}$ is computed at the order 2 from the values $c^A_{\Gamma^h}$, c^A_1, and c^A_2, still using the ghost fluid method and quadratic extrapolation:

$$\partial_x^{\Gamma^h}\, c^A_{\Gamma^h} = \frac{c^A_1 - c^s}{2\,h} = \frac{-3\, c^A_{\Gamma^h} + 4\, c^A_1 - c^A_2}{2\,h},$$

where c^s is a ghost value, which is extrapolated at the order 3 from $c^A_{\Gamma^h}$, c^A_1, and c^A_2. The intermediate values c^A_1 and c^A_2 are then interpolated at the order 3 from the known values of neighboring points (see Fig. 9(a)). To ensure the continuity in the stencil arrangements, at the

points A and B for instance, the *direct* x-derivative $\partial_x^{\Gamma^h} c^B_{\Gamma^h}$ is computed in the same way:

$$\partial_x^{\Gamma^h} c^B_{\Gamma^h} = \frac{-3\, c^B_{\Gamma^h} + 4\, c^B_1 - c^B_2}{2\, h},$$

where the intermediate values c^B_1 and c^B_2 are interpolated from the known values $c_{i,j}$, $c_{i+1,j}$ and $c_{i+2,j}$, which gives

$$\partial_x^{\Gamma^h} c^B_{\Gamma^h} = \frac{-3\, c^B_{\Gamma^h} + 0,5\, \theta_x\, (5 + 3\, \theta_x)\, c_{i,j} - (3\, \theta_x^2 + 2\, \theta_x - 4)\, c_{i+1,j} - 0,5\, (1 - \theta_x)\, (2 + 3\, \theta_x)\, c_{i+2,j}}{2\, h}.$$

Thus, if θ_x tends to 0, both points $x^A_{\Gamma^h}$ and $x^B_{\Gamma^h}$ converge towards the point $x_{i,j}$ and both stencils of $\partial_x^{\Gamma^h} c^A_{\Gamma^h}$ and $\partial_x^{\Gamma^h} c^B_{\Gamma^h}$ tend to

$$\partial_x^{\Gamma^h} c_{\Gamma^h} = \frac{-3\, c_{i,j} + 4\, c_{i+1,j} - c_{i+2,j}}{2\, h},$$

which defines the stencil continuity. An example of complete stencil is shown in Fig. 9(a).

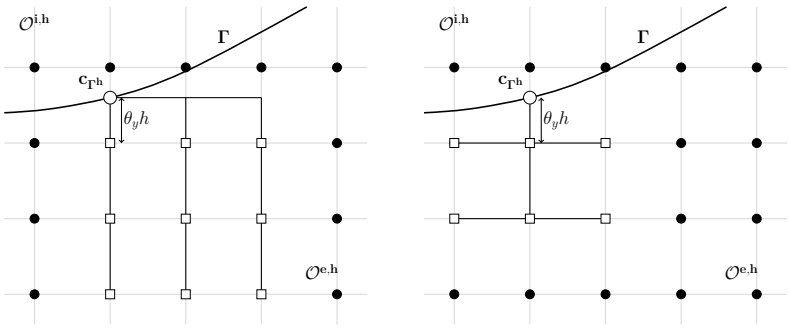

(a) Complete stencil with our modified method.

(b) Stencil with the native method.

Figure 9: Two different discretizations of the Neumann boundary condition.

The flux condition (1c) on the interface is then given by

$$\partial_x^{\Gamma^h} c_{\Gamma^h}\, n_x^{\Gamma^h} + \partial_y^{\Gamma^h} c_{\Gamma^h}\, n_y^{\Gamma^h} = -g^{\Gamma^h}, \tag{43}$$

where g^{Γ^h} is known at the order 2 at least. The normal components $n_x^{\Gamma^h}$ and $n_y^{\Gamma^h}$ are interpolated at the order 2. Thus, the required value c_{Γ^h} is obtained from (43) and can be introduced in expression (42) to compute the numerical solution in the exterior domain. This continuous approach is different from the approach of Cisternino and Weynans. It avoids considering new interface unknowns and is stable when the interface is very close to a grid point. However, it is worth noting that the stencil is three point larger than in the native method and that the code parallelization needs an additional layer (Fig. 9).

3.1.2 Interior static problem with a Dirichlet boundary condition.

The interior problem, that stands for the signal diffusion, is solved using the usual discretization of the Laplace operator at the *regular* grid points and a scheme built from linear extrapolations of

the ghost values, at the points near the interface. This scheme has been studied by Gibou *et al.* in [5]. As in the previous paragraph 3.1.1, we provide the discretization for the example of Figure 7:

$$\partial^h_{xx}\sigma^h_i = \frac{\sigma^h_{i+1} - 2\,\sigma^h_i + \sigma^h_{i-1}}{h^2}, \qquad \text{at the regular points of } \mathcal{O}^{i,h}, \tag{44}$$

$$\partial^h_{xx}\sigma^h_i = \frac{1}{h^2}\,\sigma^h_{i+1} - \frac{1+\theta_x}{\theta_x h^2}\,\sigma^h_i + \frac{1}{\theta_x h^2}\,\sigma_{\Gamma^h}, \qquad \text{in } \mathcal{O}^{i,h}, \text{ near } \Gamma. \tag{45}$$

As pointed out by Gibou *et al.*, the linear extrapolation of the ghost value gives a non-consistent second derivative (45). However, the authors numerically highlighted that the use of an inconsistent scheme near the interface does not obstruct the second order accuracy of the method. The interface values σ_{Γ^h} are directly obtained from the Dirichlet boundary condition if the data is exactly known on the interface. If it is implicitely known from an exterior field, as in our study, the previous remark ensures that an accuracy of order 2 on the boundary data c^h preserves the second order accuracy on σ^h. Thus, σ_{Γ^h} is computed by linear extrapolation from values of c^h. Finally, the approximate velocity $\mathbf{v}^h$, which is the numerical gradient of σ^h, is computed with

$$\partial^h_x u_i = \frac{u_{i+1} - u_{i-1}}{2\,h}, \qquad \text{at the regular points of } \mathcal{O}^{i,h}, \tag{46}$$

$$\partial^h_x u_i = \frac{u_{i+1} - u_i}{h}, \qquad \text{in } \mathcal{O}^{i,h}, \text{ near } \Gamma, \tag{47}$$

where (47) is a usual first order discretization of the first derivative at the point near the interface. In coherence with the computation of σ^h, it is built with the ghost fluid method and linear extrapolations of the ghost value.

3.2 Issues of the dynamics: interface location and velocity extension

At each numerical time, the coupling of the exterior and the interior problems gives the velocity of the interface. Then, the level set function, that defines implicitely the interface, is advected with the usual forward Euler scheme, by discretizing the gradient of ψ with a WENO5 scheme [11, 7]. However, two main issues arise. As the interface moves at each time iteration, we need first to update the value of θ_x and θ_y that are used to solve the static problems. Secondly, the velocity, which is defined only in the interior area, needs to be extended to transport the level set function in an appropriate way.

3.2.1 Computation of the distance to the interface

We have mentioned that the Dirichlet problem is second order accurate if the boundary condition is also second order accurate. Thus, a second order accuracy on the interface location is consistent with this requirement, which means that θ_x and θ_y should be computed at the order 1 at least. For instance, the computation of θ_x could be given by

$$\theta_x = \frac{\psi_i}{\psi_i - \psi_{i-1}}, \qquad \text{if } x_{\Gamma^h} \in [x_{i-1}, x_i], \tag{48}$$

$$\theta_x = \frac{-\psi_i}{\psi_{i+1} - \psi_i}, \qquad \text{if } x_{\Gamma^h} \in [x_i, x_{i+1}], \tag{49}$$

where ψ_i and ψ_{i-1} in (48), or ψ_i and ψ_{i+1} in (49) are of opposite sign. However, computing θ_x at a given numerical time from ψ, that is already second order accurate, adds another second

order disruption on the interface location at each subsequent iteration. In order to avoid the accumulation of these errors, we choose to compute θ_x at the order 3. This is consistent with the fact that the third order extrapolations for the Shortley-Weller scheme require a third order accuracy on the interface location.
ψ^h is therefore approximated with a third order interpolation polynomial P in the Lagrange form. Denoting by $\alpha\, h$ the distance between x_i and any point x_α of the x-axis, the polynomial P can be written as a function of α:

$$\begin{aligned} P(\alpha) =& \frac{1}{6}(\psi^h_{i-2} - 3\psi^h_{i-1} + 3\psi^h_i - \psi^h_{i+1})\alpha^3 + \frac{1}{2}(\psi^h_{i-1} - 2\psi^h_i + \psi^h_{i+1})\alpha^2 \\ &+ \frac{1}{6}(-\psi^h_{i-2} + 6\psi^h_{i-1} - 3\psi^h_i - 2\psi^h_{i+1})\alpha + \psi^h_i. \end{aligned} \tag{50}$$

Then, θ_x is solution of

$$P(\alpha) = 0,$$

and is computed with the Newton's method, for which the initial term α_0 is computed with (48)-(49).

3.2.2 Velocity extension

The extension of the velocity is a crucial point of the numerical method. The level set function can be transported without generating discontinuities near the interface only if the velocity field is smoothly defined across the interface and on the whole domain. It therefore has to be extended on each area, from the interface. Several ways of extending the velocity beyond the interface are possible. For instance, we can mention the *fast marching method*, introduced by Adalsteinsson *et al.* in [1] or some *narrow band* approaches with level set reinitialization, as in [12]. In this study, we use a PDE method that is consistent with our overall PDE-based approach and avoids the time-consuming process of level set reinitialization at each iteration. More precisely, we generate an extended velocity field $\tilde{\mathbf{v}}$ in the whole domain by solving

$$\nabla\tilde{\mathbf{v}} \cdot \nabla\psi = 0, \qquad \text{on } \Omega, \tag{51}$$

$$\tilde{\mathbf{v}} = \mathbf{v}, \qquad \text{on } \Gamma, \tag{52}$$

which means that each component of the extended velocity will be constant along the normal directions. The equation is discretized component by component, introducing the discrete gradient operator $\nabla^{\mathcal{E}}$, which is based on *upwind* derivatives (from the interface to the rest of the area). For example, to compute the x-component of the extended velocity $\tilde{v}^h_x$ near the interface, as shown in Figure 10, we solve

$$\partial^{\mathcal{E}}_x \tilde{v}^h_{x,i} = \frac{v^h_{x,\Gamma^h} - \tilde{v}^h_{x,i}}{\theta_x\, h},$$

where v^h_{x,Γ^h} is linearly extrapolated from the values of v^h_x in $\mathcal{O}^{i,h}$.
The classical first order upwind derivatives are used at the other points of $\mathcal{O}^{i,h}$ and $\mathcal{O}^{e,h}$.

3.3 Numerical validations

We simultaneously present two test-cases in order to validate the numerical method and give convergence results. The simulations are performed from a sequential code. The linear systems are inverted thanks to a BiCGStab method. The computational domain is $[-0.5, 0.5]^2$. The

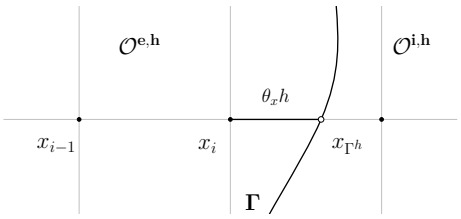

Figure 10: Example of a forward upwind x-derivatives near the interface.

main difficulty in validating the numerical method lies in the unavailability of any analytical solution, due to the strong non-linearity of the problem. We therefore compare each solution to a reference solution that is performed on a 500×500 mesh. Errors are computed at the final time $T = 1$, when they are supposed to be maximal. Note that errors on ψ^h are computed on a tubular area around the interface Γ^h, so that the ridges generated by the velocity extension are avoided and do not disturb the convergence rate computation. The convergence rates are computed by linear regression, from the comparison between the errors on the current grid and the coarsest grid. They are shown in graphs in logarithmic scale. For both cases, we define ψ at the initial time as the signed-distance function of level 0 the circle of center $(0, 0)$ and radius 0.3. At each numerical time, the boundary data are given by

- test-case 1:

$$\forall (r,\theta) \in \Gamma, \quad g_1(r,\theta) = \begin{cases} 0.05 + 3\,\exp\left(\dfrac{0.1}{(\theta + \frac{10\,\pi}{15})\,(\theta + \frac{8\,\pi}{15})}\right) & \text{if } \frac{-10\,\pi}{15} < \theta < \frac{-8\,\pi}{15}, \\ 0.05 + 2\,\exp\left(\dfrac{0.1}{(\theta + \frac{7\,\pi}{15})\,(\theta + \frac{5\,\pi}{15})}\right) & \text{if } \frac{-7\,\pi}{15} < \theta < \frac{-5\,\pi}{15}, \\ 0.05 & \text{otherwise.} \end{cases} \tag{53}$$

- test-case 2:

$$\forall (x,y) \in \Gamma, \quad g_2(x,y) = 0.1\,\left[2 + \cos\left(3\,\pi\,(x+y)\right)\,\cos\left(\pi\,(x+0.3)\right)\right]. \tag{54}$$

At each time, the functions g_1 and g_2 satisfy the hypothesis (4), as shown in Figure 11 at the initial time.

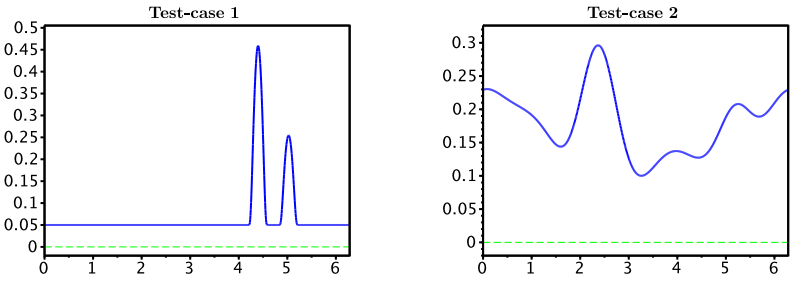

Figure 11: Functions g^0 with respect to θ.

Plots of the reference solutions σ^h at $t = 1$ (after 159 iterations for Test-case 1, 199 iterations for Test-case 2) are provided in Fig. 12 and give the general shapes of the cell at the end of

mesh	N	c^h error L^∞	order	σ^h error L^∞	order	ψ^h error L^∞	order
test-case 1							
64×64	21	$3.779\,10^{-4}$	-	$5.897\,10^{-4}$	-	$2.894\,10^{-3}$	-
96×96	31	$1.188\,10^{-4}$	2.86	$1.866\,10^{-4}$	2.84	$2.008\,10^{-3}$	0.90
144×144	46	$5.644\,10^{-5}$	2.34	$7.423\,10^{-5}$	2.56	$1.177\,10^{-3}$	1.11
216×216	69	$9.449\,10^{-5}$	1.14	$7.092\,10^{-5}$	1.74	$6.925\,10^{-4}$	1.18
324×324	103	$4.309\,10^{-5}$	1.34	$3.476\,10^{-5}$	1.75	$5.980\,10^{-4}$	0.97
test-case 2							
64×64	27	$2.391\,10^{-4}$	-	$3.191\,10^{-4}$	-	$1.775\,10^{-3}$	-
96×96	40	$1.598\,10^{-4}$	0.99	$1.518\,10^{-4}$	1.83	$1.079\,10^{-3}$	1.23
144×144	59	$7.770\,10^{-5}$	1.39	$8.514\,10^{-5}$	1.63	$6.180\,10^{-4}$	1.30
216×216	87	$4.852\,10^{-5}$	1.31	$4.447\,10^{-5}$	1.62	$3.251\,10^{-4}$	1.40
324×324	130	$1.687\,10^{-5}$	1.63	$2.054\,10^{-5}$	1.69	$1.340\,10^{-4}$	1.59

Table 1: Numerical errors and convergence rates for Test-cases 1 and 2.

each simulation. The convergence results are given on Table 1 and in Figure 13. As reported by

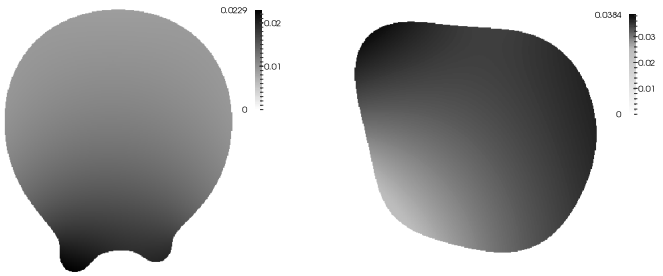

Figure 12: Plots of σ^h at t=1 for test-cases 1 (left) and 2 (right).

Table 1, we observe a first order numerical convergence for the unknowns c^h, σ^h and ψ^h of both problems, in maximum norm.

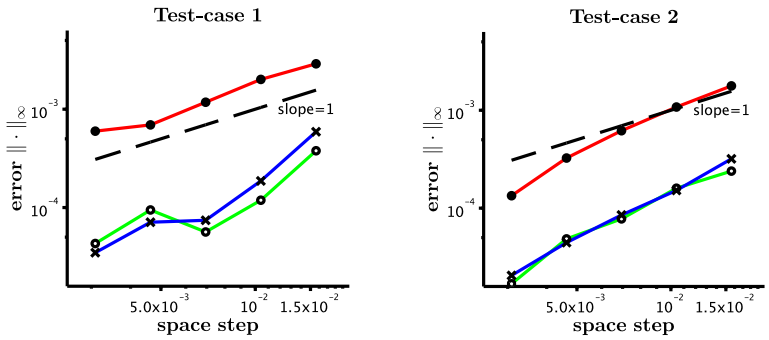

Figure 13: Convergence curves in L^∞-norm (● ψ^h, ○ c^h, ✖ σ^h).

The property of free-divergence velocity results in a good conservation of volume (see Figure 14), since variations are lower than 0.1%, of the order of h.

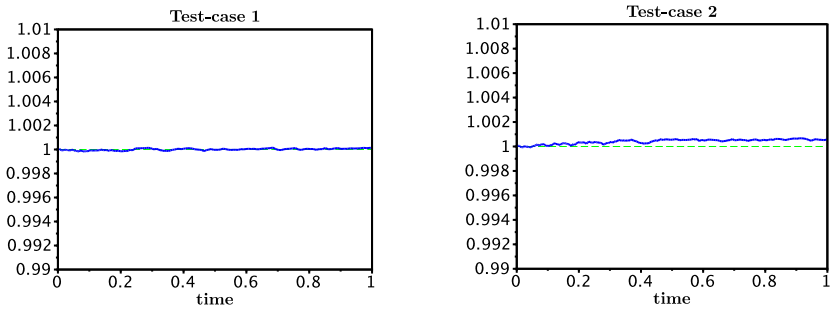

Figure 14: Volume conservation.

In order to stress Hypothesis (4), we perform the same simulations just by adding a constant (-0.1) to the data g_1 and g_2 given by (53) and (54). These new data do not verify the positivity condition and instabilities appear on the interface, at some locations where the boundary data is negative or null (Figures 15–16). In particular, Figure 15 shows that, for Test-case 2, g_2 is null at

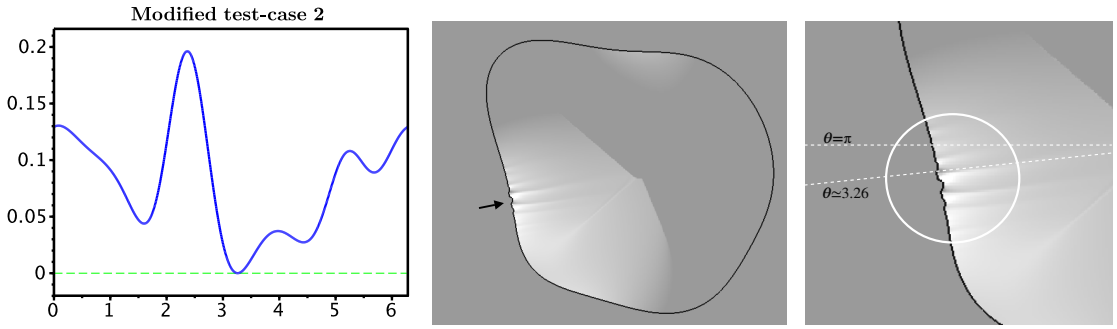

(a) Modified datum g_2.

(b) Test-case 2 at $t = 1$ (242 iterations).

(c) Zoom near the instabilities at $t = 1$.

Figure 15: Modified datum g_2 and numerical instabilities due to the violation of the hypothesis (4). Light areas indicate higher contraction velocities. Black arrows show instabilities. In Fig. 15(c), the zoom shows that instabilities occur in the region where the datum vanishes.

the point $\theta \simeq 3.26$ and it can be seen in Figure 15(b) that instabilities appear around this position and propagate along the interface. As regards Test-case 1, g_1 does not verify the condition of well-posedness on large areas and the instabilities appear, especially in the regions where the contraction velocity is higher as depicted by the white areas in Fig. 16(b). These observations seem to validate numerically Hypothesis 4 of strict positivity as a necessary condition to get a well-posed problem.

3.4 Biological model behavior: invadopodia and pseudopodia simulations

We present some visualizations of protusion formation, invadopodia and pseudopodial structures, in order to study some behaviors of the model.

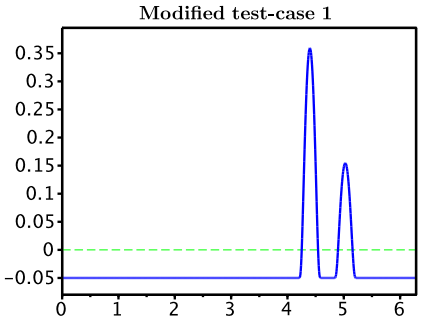

(a) Modified g_1.

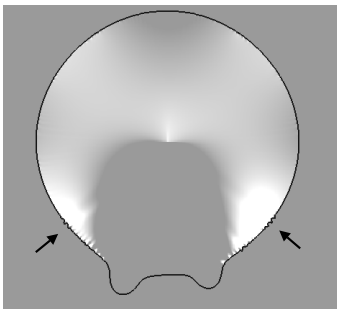

(b) Test-case 1 at $t = 0.36$ (114 iterations).

Figure 16: Modified datum g_1 and numerical instabilities due to the violation of the hypothesis (4). Light areas indicate higher contraction velocities. Black arrows show instabilities.

3.4.1 Problem 1: invadopodia.

The initial cell is an ellipse of radii 0.4 and 0.15. The exterior medium is assumed to be homogeneously composed of extracellular matrix, whose concentration value is constant and included with the MMP concentration in the function g, given as the trace on Γ of

$$\forall (r,\theta) \in \Omega, \quad G(r,\theta) = \begin{cases} 0.001 + \exp\left(\dfrac{0.1}{(\theta + \frac{9\,\pi}{16})\,(\theta + \frac{7\,\pi}{16})}\right) & \text{if } \frac{-9\,\pi}{16} < \theta < \frac{-7\,\pi}{16}, \\ 0.001 & \text{otherwise.} \end{cases} \tag{55}$$

The simulation is performed until the final time $T = 3$, for 127 iterations. We can observe the formation and growth of the invadopodium (Fig. 17(a)-17(d)). As the MMPs are very localized, the ligands are locally produced and accumulate along the protrusion (Fig. 17(e)). As expected, they create a gradient of the cytoplasmic signal at the invadopodium (Fig. 17(f)), resulting in its growth. The cell contracts in the areas that are not protrusive. This observation is supported by the normal velocity values, that show protrusive and contraction areas. This phenomenon can be mathematically explained by the divergence-free velocity, which results in a constant volume of the cell (Fig. 18). As the protrusion occurs only on a small area of the interface, the contraction area is large and the contraction velocities are weak. Consequently, the contraction movement is barely perceptible. Note that, by construction, the boundary data g behaves in time as if the area of MMP accumulation expands on the membrane as the protrusion extends. As a result, the protrusion velocity decreases, indicating a tendency to invadopodium stabilization (Fig. 19).

3.4.2 Problem 2: pseudopodia-like projection.

For the pseudopodia simulation, we use the model including modifications given by (3). The initial cell is an ellipse of radii 0.24 and 0.14, and center $(-0.15, 0)$. The simulation is performed with the data g given by

$$g(-0.5, y) = 0.1, \qquad g(0.5, y) = 0.4 \qquad \forall y \in [-0.5, 0.5], \tag{56a}$$

$$g(x, -0.5) = g(x, 0.5) = 0.25 + 0.3\,x, \qquad \forall x \in [-0.5, 0.5]. \tag{56b}$$

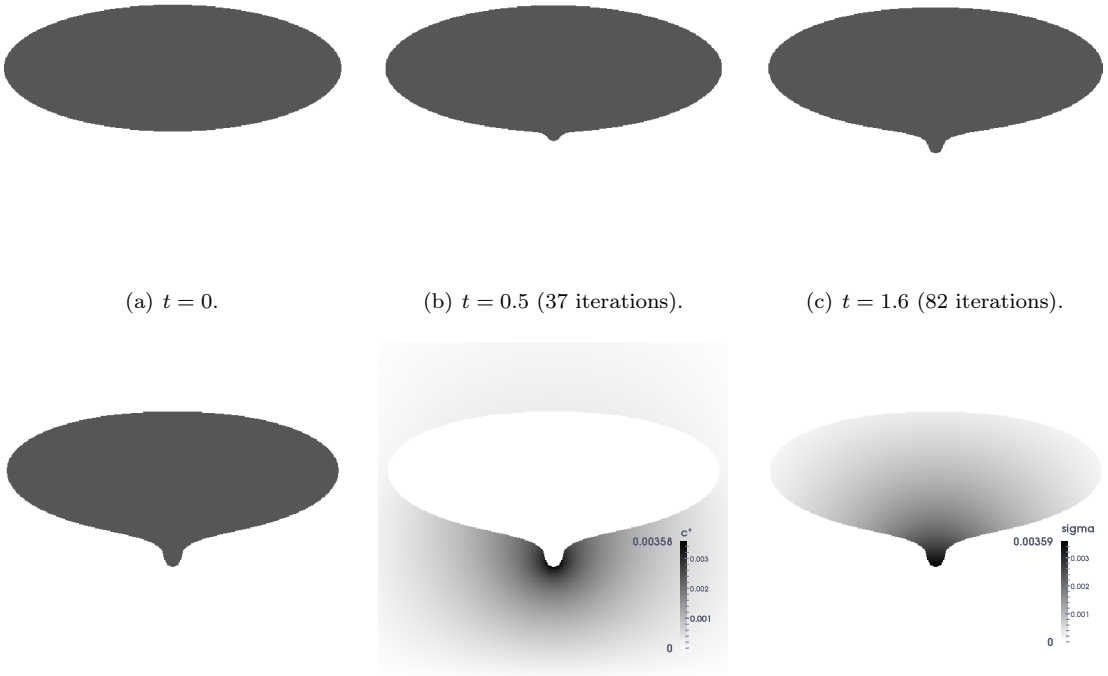

(a) $t = 0$.

(b) $t = 0.5$ (37 iterations).

(c) $t = 1.6$ (82 iterations).

(d) Cell shape at the final time $t = 3.0$ (127 iterations).

(e) Ligand concentration (c^h) at $t = 3.0$.

(f) Cytoplasmic signal (σ^h) at $t = 3.0$.

Figure 17: Simulation of an invadopodium formation.

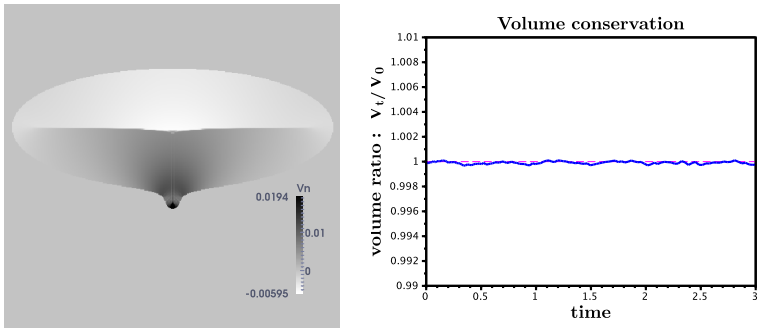

Figure 18: Normal velocity ($t = 1.2$) and volume conservation with respect to time. **Left:** the dark areas are for outcoming velocity (protrusion), the light areas are for incoming velocity (contraction). **Right:** The variations in volume are less than 0.05%.

The localization function κ is given at each time t^n as a function of σ:

$$\kappa^n = 0.001 + 0.05\ (1 + \tanh\left(\lambda(\sigma^n - \bar{\sigma}^n)\right))\,. \tag{57}$$

The signal σ gives the polarization of the cell, generated by the external gradient, and the direction of the protrusion. However the velocity can exist only in the area where the proteins

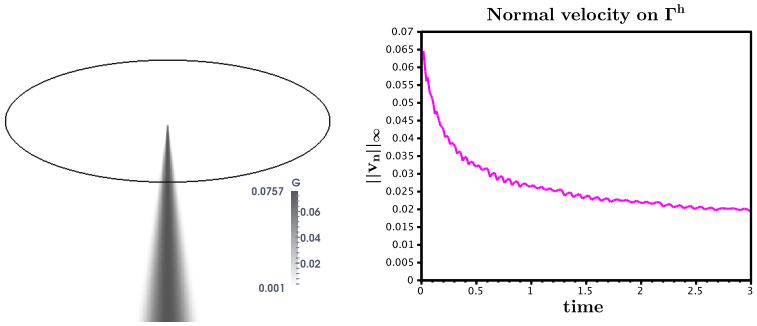

Figure 19: Stabilization of the invadopodium (right), related to the time-dependent boundary data, given at each time by the trace of G (left).

required for the actin polymerization are located, which is described by (57). The threshold $\bar{\sigma}^n$ delimits the areas with and without proteins. As these areas evolve as the protrusion grows, we define $\bar{\sigma}$ as a time-dependent linear interpolation of the extrema of σ:

$$\bar{\sigma}^n = (0.2 - 0.03\,t^n)\,\sigma_{min} + (0.8 + 0.03\,t^n)\,\sigma_{max}.$$

The slope of the curve at the limit of both areas is given by the parameter λ also defined from the extrema of σ:

$$\lambda = \frac{10}{\sigma_{max} - \sigma_{min}}.$$

The simulation is performed on a 500×500 grid until the final time $T = 5$, for 320 iterations. We provide plots of the cell shape during the simulation in Figure 20. The blood vessel is on the

(a) $t = 0$. (b) $t = 1.6$ (117 iterations). (c) $t = 5$ (320 iterations).

Figure 20: Simuation of pseudopodia formation.

right edge of the computational domain. The gradient of chemoattractant polarizes the cell from the left to the right, that leads to the formation of the protrusion on the right of the cell and to its growth towards the blood vessel. The pseudopodium width depends only on the definition of the localization function κ and more precisely on the threshold $\bar{\sigma}$. Since the velocity is not divergence-free, the pseudopodium growth results in an increased volume (Fig. 21(a)). As the cell elongates on a wide leading front, the distribution of the signal spreads out and the normal velocity decreases (Fig. 21(b)).

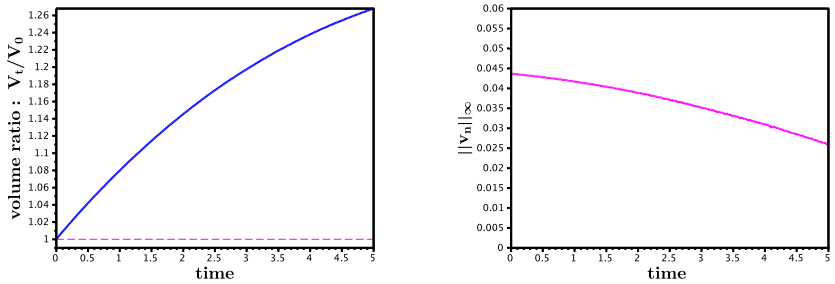

(a) Increase in volume.

(b) Decrease in normal velocity.

Figure 21: Behavior of the model for pseudopodia formation.

4 Discussion and perspectives

Our *core* model for protrusion formation under external gradient, takes the cytoplasmic membrane into account as a free boundary. It has been proved that the free boundary problem is well-posed under a sign condition (4) that has been numerically validated. Despite the simplicity of the model, the numerical methods have to be very accurate to get the consistency of the discretized problem.
Numerical simulations provide protrusion–like shapes, validating the derivation of the model. We emphasize that these are the first steps towards a precise description of cell protrusion formation. It is worth noting that the numerical data are built in order to achieve satisfying protrusion shapes. Moreover, such shapes are only rough approximates of the MMP concentration and cytoplasmic protein localization. In the case of invadopodia, cytoplasmic and membrane dynamics of MMPs remain to be explored to obtain a realistic time-dependent function g, in the purpose, for instance, to calibrate the model or study the stabilization of invadopodia, as in [18]. The issue of the divergence-free velocity also arises: does the cell deform at constant volume or is the membrane extended? Regarding pseudopodia, it seems easier to get a realistic boundary data since it just corresponds to the concentration of chemoattractant released by the neighboring blood vessel. Moreover, numerical simulations are more straightforward because larger protrusions require less grid refinement and generate less numerical instabilities. However, the issue of the cell polarization and the cytoplasmic protein distribution, that is roughly approximated by the function κ in our study, also remains to deepen.
Note that in order to achieve a complete migratory behavior, it should be necessary to introduce many other biological processes, especially cell-collagen adhesions and myosin-induced contractility. Then we could obtain more realistic simulations by combining pseudopodia and invadopodia for a cell that would migrate in a matrix of collagen fibers. In conclusion, we have proposed and studied theoretically and numerically a *core* model that is a new step in the modeling of protrusion formation at the cellular level. This topic is the cornerstone of the cell migration understanding, especially as regards the cancer cell invasion and migration. However, many biological issues, such as MMPs and cell polarization dynamics or velocity definition, and mathematical issues, like 3D-analysis and numerical analysis, remain to be further studied.

Acknowledgements

This study has been carried out with financial support from the JSPS Core to Core program Advanced Research Networks.

O.G and C.P has been partly supported by the French National Research Agency (ANR) in the frame of the "Investments for the future" Programme IdEx Bordeaux - CPU (ANR-10-IDEX-03-02).

Numerical simulations presented in this paper were carried out using the PLAFRIM experimental testbed, being developed under the Inria PlaFRIM development action with support from LABRI and IMB and other entities: Conseil Régional d'Aquitaine, FeDER, Université de Bordeaux and CNRS (see https://plafrim.bordeaux.inria.fr/).

The authors would like to thank very warmly Professor Thierry Colin for his advices and suggestions that were helpful in the analytical and numerical study of the cell migration problem.

A The quasistatic 2–phase Stefan problem

In this Appendix we consider the quasistatic 2–phase Stefan problem set in the domain Ω defined as in Fig. 4. We use the same notation as before for the geometry. Let g be a given function defined in $\mathbb{R}^+ \times \mathbb{R}^2$. The PDE system satisfied by ζ, $c^\star$, and σ reads

$$\zeta|_{t=0} = \zeta_0, \quad \text{and} \quad \partial_t \zeta = \nabla(\sigma - c^\star)(\zeta(t,\theta)), \quad \forall t > 0, \ \ \forall \theta \in \mathbb{R}/2\pi\mathbb{Z}, \tag{58a}$$

where $\forall t \geq 0$, one has

$$\Delta c^\star = 0, \quad x \in \mathcal{O}_t^e, \tag{58b}$$
$$c^\star|_{\partial\Omega} = 0, \quad c^\star|_{\Gamma_t} = g|_{\Gamma_t}, \tag{58c}$$
$$\Delta \sigma = 0, \quad t \in [0,T], \ \ x \in \mathcal{O}_t^i, \tag{58d}$$
$$\sigma|_{\Gamma_t} = c^\star|_{\Gamma_t}. \tag{58e}$$

From the numerical point of view, since Dirichlet conditions are imposed on both sides of Γ_t, our numerical schemes can be easily used with the same order of accuracy. In the following we show how to obtain the well-posedness result:

Theorem 19 (Well-posedness of the quasistatic 2–phase Stefan problem)**.** *Let Ω be a smooth domain of $\mathbb{R}^2$ which strictly contains the unit disk, and denote by Γ_0 the initial location of the interface, given as a perturbation of the unit circle : $\Gamma_0 = \{e^{i\theta} + \xi_0,\ \theta \in \mathbb{T}\}$.*

Let $s \geq 3$, and let $g \in W^{1,\infty}(\mathbb{R}^+; H^{s+3/2}(\Omega))$ such that for a given $\alpha > 0$, and $M > 0$,

$$\nabla g(t,x) \cdot \zeta_0^\perp \geq \alpha > 0, \qquad \|g\|_{W^{1,\infty}(\mathbb{R}^+; H^{s+3/2})} \leq M, \qquad \text{with } \zeta_0(\theta) = e^{i\theta}. \tag{59}$$

There exist $\delta > 0$ and $T > 0$ small enough such that if

$$\|\xi_0\|_{H^s(\mathbb{T})} \leq \delta,$$

then, there exists a unique solution $(\zeta, c^\star, \sigma)$ on $(0,T)$ to problem (58) such that

$$\zeta \in L^\infty(0,T; H^s(\mathbb{T})) \cap L^2(0,T; H^{s+1}),$$

and for almost any $t \in (0,T)$,

$$c^\star \in H^{s+1/2}(\mathcal{O}_t^e), \qquad \sigma \in H^{s+1/2}(\mathcal{O}_t^i).$$

A.1 Equivalent problem on the torus $\mathbb{T} = \mathbb{R}/2\pi\mathbb{Z}$

We write an equivalent problem set on the torus $\mathbb{T} = \mathbb{R}/2\pi\mathbb{Z}$. Deriving with respect to θ the Dirichlet traces of σ and $c^\star$ on Γ_t, we get:

$$\partial_t\zeta \cdot \partial_\theta\zeta = \nabla(\sigma - c^\star)|_\zeta \cdot \partial_\theta\zeta = 0.$$

Then, setting

$$X_1 = \xi \cdot \partial_\theta\zeta_0, \quad X_2 = \xi \cdot \partial_\theta\zeta_0^\perp,$$

we get the first equation which corresponds to (30) for the cell migration problem:

$$(1 + X_2 + \partial_\theta X_1)\partial_t X_1 = (X_1 - \partial_\theta X_2)\partial_t X_2. \tag{60}$$

Then, thanks to Lemma 7, we get:

$$\begin{aligned}
\nabla c^\star \cdot \partial_\theta\zeta_0 &= \mathcal{L}_{\rm e}(\nabla c^\star \cdot \partial_\theta\zeta_0^\perp),\\
&= \mathcal{L}_{\rm e}(\nabla\sigma \cdot \partial_\theta\zeta_0^\perp) - \mathcal{L}_{\rm e}(\partial_t\xi \cdot \partial_\theta\zeta_0^\perp),\\
&= \mathcal{L}_{\rm e}(\mathcal{L}_{\rm i}\nabla\sigma \cdot \partial_\theta\zeta_0) - \mathcal{L}_{\rm e}(\partial_t\xi \cdot \partial_\theta\zeta_0^\perp),\\
&= \mathcal{L}_{\rm e}(\mathcal{L}_{\rm i}\nabla c^\star \cdot \partial_\theta\zeta_0) + \mathcal{L}_{\rm e}\mathcal{L}_{\rm i}(\partial_t\xi \cdot \partial_\theta\zeta_0) - \partial_t\xi \cdot \partial_\theta\zeta_0^\perp.
\end{aligned}$$

Now observe that around $\xi = 0$, the operator writes:

$$\mathcal{L}_{\rm e}\mathcal{L}_{\rm i} \sim \mathcal{H}^2 = \mathcal{P}_0 - 1,$$

thus for ξ small enough, $(1 - \mathcal{L}_{\rm e}\mathcal{L}_{\rm i}) \sim 2 - \mathcal{P}_0$, which is invertible. Therefore $(1 - \mathcal{L}_{\rm e}\mathcal{L}_{\rm i})$ is invertible for ξ small enough and

$$(1 - \mathcal{L}_{\rm e}\mathcal{L}_{\rm i})^{-1} \sim \frac{1}{2}(1 + \mathcal{P}_0),$$

and thus we get:

$$\nabla c^\star \cdot \partial_\theta\zeta_0 = \mathcal{A}(-\partial_t X_2 + \mathcal{L}_{\rm i}(\partial_t X_1)), \tag{61}$$

where

$$\mathcal{A} = \{1 - \mathcal{L}_{\rm e}\mathcal{L}_{\rm i}\}^{-1}\,\mathcal{L}_{\rm e}\,(\mathcal{L}_{\rm i} - 1) \sim -\frac{1}{2}(1 - \mathcal{P}_0 + \mathcal{H}).$$

Similarly, we obtain:

$$\begin{aligned}
\nabla c^\star \cdot \partial_\theta\zeta_0^\perp &= -\partial_t\xi \cdot \partial_\theta\zeta_0^\perp + \nabla\sigma \cdot \partial_\theta\zeta_0^\perp,\\
&= -\partial_t\xi \cdot \partial_\theta\zeta_0^\perp + \mathcal{L}_{\rm i}(\nabla\sigma \cdot \partial_\theta\zeta_0),\\
&= -\partial_t X_2 + \mathcal{L}_{\rm i}(\partial_t X_1) + \mathcal{L}_{\rm i}(\mathcal{L}_{\rm e}(\nabla c^\star \cdot \partial_\theta\zeta_0^\perp),
\end{aligned}$$

and thus

$$\nabla c^\star \cdot \partial_\theta\zeta_0^\perp = \mathcal{B}\,(-\partial_t X_2 + \mathcal{L}_{\rm i}(\partial_t X_1))\,, \tag{62}$$

where

$$\mathcal{B} = (1 - \mathcal{L}_{\rm i}\mathcal{L}_{\rm e})^{-1} \sim \frac{1}{2}(1 + \mathcal{P}_0).$$

We are now ready to obtain the second equation, which corresponds to equation (31). Since

$$\begin{aligned}\nabla g \cdot \partial_\theta \zeta &= \nabla c^\star \cdot \partial_\theta \zeta_0 + \nabla c^\star \cdot \partial_\theta \xi,\\ &= (1 + \partial_\theta \xi \cdot \partial_\theta \zeta_0)\, \nabla c^\star \cdot \partial_\theta \zeta_0 + \partial_\theta \xi \cdot \partial_\theta \zeta_0^\perp\, (\nabla c^\star \cdot \partial_\theta \zeta_0^\perp),\\ &= \{(1 + X_2 + \partial_\theta X_1)\mathcal{A} + (\partial_\theta X_2 - X_1)\mathcal{B}\}\, (-\partial_t X_2 + \mathcal{L}_{\rm i}(\partial_t X_1))\,,\end{aligned}$$

hence we infer

$$\begin{aligned}&\{(1 + X_2 + \partial_\theta X_1)\mathcal{A} + (\partial_\theta X_2 - X_1)\mathcal{B}\}\, (-\partial_t X_2 + \mathcal{L}_{\rm i}(\partial_t X_1))\\ =&(1 + X_2 + \partial_\theta X_1)\nabla g \cdot \zeta_0 + (\partial_\theta X_2 - X_1)\nabla g \cdot \zeta_0^\perp.\end{aligned} \tag{63}$$

A.2 Quasilinearization

Now let $(Y_i)_{i=1,\cdots,4}$ and W be defined as

$$\begin{aligned}&Y_1 = X_1, \quad Y_2 = X_2,\\ &Y_3 = \partial_\theta X_1 + X_2, \quad Y_4 = \partial_\theta X_2 - X_1,\\ &W = -\partial_t X_2 + \mathcal{L}_{\rm i}(\partial_t X_1).\end{aligned}$$

Equations (60)–(63) write now:

$$\partial_t Y_1 = -\left(1 + Y_3 - Y_4 \mathcal{L}_{\rm i}\right)^{-1} W \sim_{\xi \sim 0} -W, \tag{64a}$$

$$\partial_t Y_2 = -W - \mathcal{L}_{\rm i}\left(1 + Y_3 - Y_4 \mathcal{L}_{\rm i}\right)^{-1} W \sim_{\xi \sim 0} -(1 + \mathcal{H})W, \tag{64b}$$

$$\begin{aligned}\partial_t Y_3 &= -\partial_\theta \left(1 + Y_3 - Y_4 \mathcal{L}_{\rm i}\right)^{-1} W - W - \mathcal{L}_{\rm i}\left(1 + Y_3 - Y_4 \mathcal{L}_{\rm i}\right)^{-1} W,\\ &\sim_{\xi \sim 0} -\partial_\theta W - (1 + \mathcal{H})W,\end{aligned} \tag{64c}$$

$$\begin{aligned}\partial_t Y_4 &= -\partial_\theta W - \partial_\theta \mathcal{L}_{\rm i}\left(1 + Y_3 - Y_4 \mathcal{L}_{\rm i}\right)^{-1} W + \left(1 + Y_3 - Y_4 \mathcal{L}_{\rm i}\right)^{-1} W,\\ &\sim_{\xi \sim 0} -(1 + \mathcal{H})\partial_\theta W + W,\end{aligned} \tag{64d}$$

and on W we get

$$\{(1 + Y_3)\mathcal{A} + Y_4 \mathcal{B}\}\, W = (1 + Y_3)\, \nabla g \cdot \zeta_0 + Y_4\, \nabla g \cdot \zeta_0^\perp. \tag{64e}$$

Deriving equation (64e) with respect to time, we infer, around $\xi \sim 0$ the following non-linear PDE:

$$\partial_t W + \nabla g \cdot \zeta_0\, \partial_\theta W + \nabla g \cdot \zeta_0^\perp (1 + \mathcal{H})\partial_\theta W = f(\mathbb{Y}, g, \partial_t g, W, \partial_\theta W),$$

and we get the well-posedness in $L^\infty(0, T; H^s) \cap L^2(0, T; H^{s+1})$ under the sign condition

$$\nabla g \cdot \zeta_0^\perp \geq \alpha > 0,$$

with $g \in W^{1,\infty}(0, T; H^{s+3/2})$.

References

[1] D. Adalsteinsson and J.A Sethian. The Fast Construction of Extension Velocities in Level Set Methods. *Journal of Computational Physics*, 148(1):2–22, 1999.

[2] M. Cisternino and L. Weynans. A parallel second order cartesian method for elliptic interface problems. *Communications in Computational Physics*, 12:1562–1587, June 2012.

[3] R. P. Fedkiw, T. Aslam, B. Merriman, and S. Osher. A Non-oscillatory Eulerian Approach to Interfaces in Multimaterial Flows (the Ghost Fluid Method). *Journal of Computational Physics*, 152(2):457–492, 1999.

[4] P. Friedl and K. Wolf. Tumour-cell invasion and migration: diversity and escape mechanisms. *Nat Rev Cancer*, 3(5):362–374, 05 2003.

[5] F. Gibou, R.P. Fedkiw, L.T. Cheng, and M. Kang. A Second-Order-Accurate Symmetric Discretization of the Poisson Equation on Irregular Domains. *Journal of Computational Physics*, 176:205–227, 2002.

[6] T. Iguchi. On the irrotational flow of incompressible ideal fluid in a circular domain with free surface. *Publ. Res. Inst. Math. Sci.*, 34(6):525–565, 1998.

[7] G-S. Jiang and C-W. Shu. Efficient Implementation of Weighted ENO Schemes. *Journal of Computational Physics*, 126(1):202–228, 1996.

[8] T. Kato. Nonlinear semigroups and evolution equations. *J. Math. Soc. Japan*, 19:508–520, 1967.

[9] D. Lannes. Well-posedness of the water-waves equations. *J. Amer. Math. Soc.*, 18(3):605–654 (electronic), 2005.

[10] H. Levine and W.-J. Rappel. The physics of eukaryotic chemotaxis. *Phys Today*, 66(2), 2013.

[11] X-D. Liu, S. Osher, and T. Chan. Weighted Essentially Non-oscillatory Schemes. *Journal of Computational Physics*, 115(1):200–212, 1994.

[12] P. Macklin and J. Lowengrub. Evolving interfaces via gradients of geometry-dependent interior Poisson problems: application to tumor growth. *Journal of Computational Physics*, 203(1):191–220, 2005.

[13] A. Mogilner. On the edge: modeling protrusion. *Current Opinion in Cell Biology*, 18(1):32–39, 2006. Cell structure and dynamics.

[14] V. I. Nalimov. The Cauchy-Poisson problem. *Dinamika Splošn. Sredy*, Vyp. 18 Dinamika Zidkost. so Svobod. Granicami:104–210, 254, 1974.

[15] S. Osher and J.A. Sethian. Fronts Propagating with Curvature Dependent Speed: Algorithms Based on Hamilton-Jacobi Formulations. *Journal of Computational Physics*, 79(1):12–49, 1988.

[16] A. Pathak and S. Kumar. Biophysical regulation of tumor cell invasion: moving beyond matrix stiffness. *Integr. Biol.*, 3:267–278, 2011.

[17] A. J. Ridley, M. A. Schwartz, K. Burridge, R. A. Firtel, M. H. Ginsberg, G. Borisy, J. T. Parsons, and A. R. Horwitz. Cell Migration: Integrating Signals from Front to Back. *Science*, 302(5651):1704–1709, 2003.

[18] T. Saitou, M. Rouzimaimaiti, N. Koshikawa, M. Seiki, K. Ichikawa, and T. Suzuki. Mathematical modeling of invadopodia formation. *J Theor Biol., 298*, pages 138–146, 2012.

[19] P.M. Schoumacher, R.D. Goldman, D. Louvard, and D.M. Vignjevic. Actin,microtubules, and vimentin intermediate filament cooperate for elongation of invadopodia. *J Cell Biol.*, 189(3):541–556, 2010.

[20] G. H. Shortley and R. Weller. The Numerical Solution of Laplace's Equation. *Journal of Applied Physics*, 9(5):334, 1938.

[21] C. Stock and A. Schwab. Role of the Na+/H+ exchanger NHE1 in cell migration. *Acta Physiologica*, 187(1–2):149–157, 2006.

[22] M. Yang, D. J. Kozminski, L. A. Wold, R. Modak, J. D. Calhoun, L. L. Isom, and W. J. Brackenbury. Therapeutic potential for phenytoin: targeting nav1.5 sodium channels to reduce migration and invasion in metastatic breast cancer. *Breast Cancer Research and Treatment*, 134(2):603–615, 2012.

[23] H. Yosihara. Gravity waves on the free surface of an incompressible perfect fluid of finite depth. *Publ. Res. Inst. Math. Sci.*, 18(1):49–96, 1982.

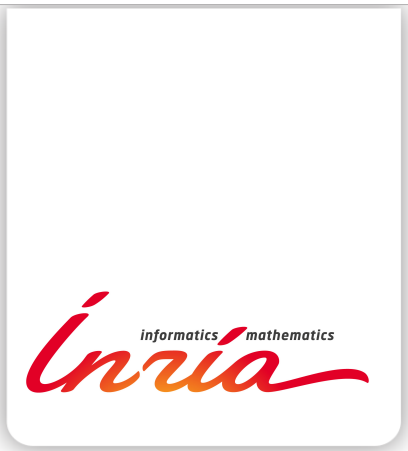

RESEARCH CENTRE
BORDEAUX – SUD-OUEST

200 avenue de la Vieille Tour
33405 Talence Cedex

Publisher
Inria
Domaine de Voluceau - Rocquencourt
BP 105 - 78153 Le Chesnay Cedex
inria.fr

ISSN 0249-6399